

**EFFECTS OF ACOUSTICS ON INDUCED DROPLET SHEDDING IN
DROPWISE CONDENSATION**

A Thesis

by

JOSE EDUARDO MEJIA

Submitted to the Office of Graduate and Professional Studies of
Texas A&M University
in partial fulfillment of the requirements for the degree of

MASTER OF SCIENCE

Chair of Committee,	Jorge L. Alvarado
Co-Chair of Committee,	Michael Pate
Committee Member,	Mark Kimber
Head of Department,	Andreas A. Polycarpou

December 2017

Major Subject: Mechanical Engineering

Copyright 2017 Jose Eduardo Mejia

ABSTRACT

Research studies over the years have confirmed that dropwise condensation is more effective than film-wise condensation since it promotes higher rates of heat transfer. However, droplet shedding in dropwise condensation still is one of the limiting steps in the overall condensation phenomena, even when using engineered surfaces. Therefore, acoustic stimuli should be considered to promote adequate droplet shedding during condensation. To that end, an acoustic system has been developed to induce droplet shedding via substrate-droplet resonance.

To understand the relationship between droplet sliding angle and body forces such as gravity and acoustic streaming, a mathematical model has been postulated capable of predicting the critical sliding angle of droplets. Recently, a mathematical physics-based model has been developed, which can predict droplet-sliding angles while using a variety of surfaces including those with hydrophobic and hydrophilic wetting characteristics. The model has been validated experimentally with and without imposing acoustic stimuli under the influence of gravity. Initially, the relationship between the sliding angle and droplet volume were investigated experimentally to obtain the contact angle hysteresis for smooth surfaces. Then, different natural frequencies of droplets were also examined to determine the best resonance mode of vibration that leads to lower-sliding angles. Experimental data show that the model can be used effectively to relate imposed resonance frequency to critical sliding angle of droplets.

Experimental results to date also show that surfaces with hydrophobic properties, depict lower condensation rates than hydrophilic surfaces. Moreover, hydrophobic surfaces depict droplets with less contact area and greater surface area on the vapor side, which lead to greater thermal resistance and lower condensation rates. While imposing vibrations to a condensation system, a surface with super-hydrophobic properties shows an enhancement in heat flux of 45%. Furthermore, heat transfer enhancement in both hydrophilic and hydrophobic surfaces can be achieved when the difference between surface temperature and ambient temperature (ΔT) is in the range of 10 to 12.5 °C. In summary, vibrations help shed smaller droplets faster, which allow for faster rate of dropwise condensation. Furthermore, vibrations help mitigate the effects of surface tension on condensation.

DEDICATION

I would like to dedicate this work to my wonderful parents, Jose Refugio Mejia Valdivia and Miriam Mejia, and to my brothers, Jose Carlos Mejia and Paola Mejia, for their outstanding support and unconditional love throughout my completion of my graduate education. To my grandparents, Teresa Valdivia Jauregui and Ramon Mejia Ortiz†, to be always for me during the difficult times throughout my education and for their unconditional love. To Dr. Jorge Alvarado for his inspiration and motivation to pursue a doctoral degree. To all my friends for their unconditional and memorable friendship, laugh, and support during my graduate education at Texas A&M.

ACKNOWLEDGEMENTS

I would like to thank my committee chair, Dr. Jorge Alvarado, and my committee members and faculty, Dr. Michael Pate, Dr. Mark Kimber, Dr. Yong-Joe Kim, and Dr. Chun-Wei Yao, for their guidance and support throughout the course of this research.

Thanks also go to my friends and colleagues and the department faculty and staff for making my time at Texas A&M University a great and unforgettable experience.

I sincerely thank for the encouragement of my family of pursuing my master's degree, Miriam Mejia and Jose Refugio Mejia Valdivia, for support and love.

CONTRIBUTORS AND FUNDING SOURCES

Contributors

This work was supervised by chair of committee, Professor Jorge Alvarado of the Department of Engineering Technology and Industrial Distribution and Dr. Chun-Wei Yao from Lamar University.

Dr. Yong-Joe Jim from the Department of Mechanical Engineering helped in the derivation and development of equation 40 as shown in Chapter 3.

All other work conducted for the thesis was completed by the student independently.

Funding Sources

Graduate study was supported by a fellowship from NSF sponsored TAMUS Louis Stokes Alliance for Minority Participation from 2015 to 2017.

NOMENCLATURE

a_0	Acceleration or amplitude of vibration excitation
F_{cap}	Capillary force
F_g	Gravitational force
F_v	Vibrational force
g	Gravitational acceleration
h	Convective heat transfer
k	Dimensionless factor of a droplet
L	Length of droplet
m	Weight of the droplet
q	Wave factor
q''	Heat flux
R	Droplet contact radius
T_s	Surface temperature
V	Volume of droplet
w	Width of droplet
α	Sliding angle
β	Aspect ratio of droplet
γ_{LG}	Surface tension
$\Delta\theta$	Contact angle hysteresis of droplet
ΔT	Temperature gradient

θ	Contact angle of droplet
θ_a	Advancing angle
θ_r	Receding angle
ρ	Density of droplet
ω	Resonance frequency

Subscript:

j	Resonance mode
L	Liquid
S	Solid
V	Vapor

TABLE OF CONTENTS

	Page
ABSTRACT	ii
DEDICATION	iv
ACKNOWLEDGEMENTS	v
CONTRIBUTORS AND FUNDING SOURCES.....	vi
NOMENCLATURE.....	vii
TABLE OF CONTENTS	ix
LIST OF FIGURES.....	xii
LIST OF TABLES	xv
1 INTRODUCTION.....	1
1.1 Motivation.....	1
1.2 Objectives	2
2 BACKGROUND AND LITERATURE REVIEW.....	4
2.1 Fundamental theory of droplet sliding model.....	4
2.1.1 Contact angles on distinctive surface wetting properties.....	5
2.1.2 Contact angle hysteresis effect	7
2.1.3 Relation between contact angles, drop shape, retention force, and sliding	8
2.2 Vibrations of liquid droplets.....	10
2.2.1 Contact line oscillation modes.....	10
2.2.2 Prediction of resonant modes of vibrations in droplets	12
2.3 Condensation heat transfer.....	15
2.3.1 Dropwise condensation.....	15
2.4 Conclusion	17
3 DEVELOPMENT OF PHYSICS BASED MATHEMATICAL MODEL FOR DROPLET SLIDING	18
3.1 Formulation of droplet sliding-off angle without imposing acoustics.....	18
3.2 Formulation of droplet sliding-off angle under the effects of imposed resonant acoustic frequencies.....	22

4 EXPERIMENTAL SETUP AND PROCEDURE.....	24
4.1 Tilting stage system for droplet sliding	25
4.2 Vibrational system for droplet sliding	27
4.3 Data acquisition system (DAQ board).....	28
4.4 Image capture system for static and dynamic droplet motion	29
4.5 Standard surfaces	29
4.6 Calibration of vibrational system.....	30
4.7 Procedures for sliding angle experiments with and without imposing acoustics to the system	33
4.7.1 Contact angle measurement	33
4.7.2 Sliding angle measurement for non-vibrational cases	34
4.7.3 Droplet aspect ratio	35
4.7.4 Resonance frequency of droplets	36
4.7.5 Sliding angle of droplets when imposing acoustics to the system.....	37
4.7.6 Measuring acceleration for validating developed physics-based mathematical models	37
4.8 Dropwise condensation.....	38
4.8.1 Description of the condensation components	40
4.8.2 Calibration of thermocouples and heat flux sensor	43
4.8.3 Dropwise condensation experiment protocols.....	45
5 RESULTS AND DISCUSSION.....	47
5.1 Validating the droplet sliding angle model without the effects of acoustics	47
5.2 Resonance frequencies and resonance modes of vibrations using the Noblin’s model	52
5.2.1 Calculated resonance frequency	52
5.2.2 Experimental resonance frequency using the first and second resonance modes of vibration	54
5.3 Validating the droplet sliding angle model under the effects of acoustics	56
5.4 Sliding angle enhancement comparison between the first and second resonance modes of vibration	62
5.5 Condensation experiments results	64
5.5.1 Heat transfer performance of standard surfaces	64
5.5.2 Heat transfer performance of standard surfaces with vibrations imposed.....	71
5.5.3 Empirical heat transfer coefficient correlations.....	81
6 CONCLUSION	85
7 FUTURE WORK	88
REFERENCES.....	89
APPENDIX A	96

A.1 Effects of friction on viscous dissipation in sliding droplet	96
A.2 Physical properties of droplets for condensation analysis	97
A.3 Sliding droplet data for silicon wafer (SiO ₂) surface case.....	100

LIST OF FIGURES

	Page
Fig. 2.1 Surface tension components and contact angle of a droplet on (a) hydrophobic surface, (b) hydrophilic surface	5
Fig. 2.2 Droplet with different wetting characteristics of (a) Cassie-Baxter condition and (b) Wenzel condition.....	7
Fig. 2.3 Depiction of contact angle hysteresis.....	8
Fig. 2.4 Plane view of liquid droplets with most common shape at an inclined plane	10
Fig. 2.5 Droplet contact schematic illustrating droplet contact angle and contact line....	12
Fig. 2.6 Droplet schematic depicting modes of vibrations of mode (a) $j = 1$ (2 nodes) and (b) $j = 2$ (4 nodes).....	14
Fig. 3.1 (a) Tilted surface at a specific droplet sliding angle α ; advancing and receding angle, and (b) experimental droplet sliding	19
Fig. 4.1 Experimental setup to validate the developed sliding models [6]	24
Fig. 4.2 Experimental setup for droplet sliding.....	25
Fig. 4.3 Tilted stage system utilized to perform droplet sliding experiments	26
Fig. 4.4 Schematic of tilting range systems	27
Fig. 4.5 Infinity Reference 860w that was utilized to impose vibrations to the system...28	
Fig. 4.6 Photron SA3 high speed camera utilized to capture droplet images	29
Fig. 4.7 Calibration input/output of the acoustic system.....	31
Fig. 4.8 Correlation between vibrational energies imposed on horizontal and along the sliding plane.....	32
Fig. 4.9 Image used for static contact angle measurement of a 10 μ L droplet on teflon ..33	
Fig. 4.10 Measurement of advancing and receding angle when the droplet starts sliding off the surface using a 10 μ L teflon.....	35
Fig. 4.11 Water droplet on inclined surface used to determine aspect ratio, β	36

Fig. 4.12 Acoustic-induced condensation system I.....	39
Fig. 4.13 Acoustic-induced condensation system II.....	39
Fig. 4.14 Peltier Thermo-Electric Cooler Module and Heatsink Assembly [42].....	40
Fig. 4.15 Fuji Electric PXR4 Temperature Controller [43]	41
Fig. 4.16 PureGuardian H8000B Ultrasonic Warm and Cool Humidifier [44]	42
Fig. 4.17 HFS-4 sandwiched between similar standard surfaces	42
Fig. 4.18 Calibration system using a heater plate	44
Fig. 4.19 Schematic of the heat flux and thermocouple calibration system.....	45
Fig. 5.1 Measurement of advancing and receding angle when droplet start sliding off the surface without imposing acoustics	48
Fig. 5.2 Relationship between droplet volume and sliding angle	49
Fig. 5.3 (a) Relationship between contact angle hysteresis and droplet volume, and (b) relationship between sliding angle and contact angle hysteresis.....	50
Fig. 5.4 Comparison of the theoretical and experimental values based on sliding terms	52
Fig. 5.5 Representation of expected droplet motion for (a) non-vibration case, (b) the first resonance mode and (c) the second resonance mode. Colored dots represent number of nodes.....	54
Fig. 5.6 Droplet resonance mode of vibrations using a 10 μ L droplet on a teflon.....	55
Fig. 5.7 Vibrations at two distinct resonance modes of a 20 μ L droplet on copper surface on an inclined plane	57
Fig. 5.8 Relationship between droplet volume and sliding angle for (a) the first resonance mode and (b) the second resonance mode	57
Fig. 5.9 The sliding angle of 20 μ L droplet at different resonant frequencies.....	58
Fig. 5.10 Comparison between the theoretical and experimental sliding angle.....	61
Fig. 5.11 Comparison in theoretical and experimental sliding angle with a R ² of 0.98...62	
Fig. 5.12 Condensation droplet size of (a) aluminum at 2.8 °C, (b) copper at 2.2 °C, (c) hydro-copper at 2.9 °C, and (d) painted metallic surface at 2.6 °C	65

Fig. 5.13 Droplet size distribution of (a) aluminum, (b) copper, (c) hydro-copper, and (d) painted metallic surface	66
Fig. 5.14 Combined droplet size distribution for all surfaces	67
Fig. 5.15 Condensation heat flux curves for non-vibration cases	71
Fig. 5.16 Hydro-copper image analysis of (a) condensate droplets without the use of vibration and (b) condensate droplets with the use of vibrations that leads to a refreshed surface area for new droplet nucleation	74
Fig. 5.17 Condensation heat flux curve comparison of copper with and without imposing vibrations to the system	77
Fig. 5.18 Condensation heat flux curve comparison of aluminum with and without imposing vibrations to the system	78
Fig. 5.19 Condensation heat flux curve comparison of hydro-copper with and without imposing vibrations to the system	78
Fig. 5.20 Condensation heat flux curve comparison of a metallic surface with and without imposing vibrations to the system	79
Fig. 5.21 Condensation convective heat transfer curve comparison of copper with and without imposing vibrations to the system	79
Fig. 5.22 Condensation convective heat transfer curve comparison of aluminum with and without imposing vibrations to the system	80
Fig. 5.23 Condensation convective heat transfer curve comparison of hydro-copper with and without imposing vibrations to the system	80
Fig. 5.24 Condensation convective heat transfer curve comparison of painted metallic surface with and without imposing vibrations to the system.....	81
Fig. 5.25 Relative error of the developed correlations based on (a) hydrophilic surfaces ($\theta < 90^\circ$ or $\pi/2$) without vibrations, (b) hydrophilic surfaces with vibrations, (c) hydrophobic surfaces ($\theta > 90^\circ$ or $\pi/2$) without vibrations, (d) hydrophobic with vibrations, (e) hydro-copper correlation without vibrations, and (f) hydro-copper correlation with vibrations.....	84
Fig. A.1 Typical droplet in dropwise condensation	97
Fig. A.2 The sliding angle of different droplet volumes on SiO ₂	101

LIST OF TABLES

	Page
Table 4.1 Description of surface wetting properties for standard surfaces	30
Table 5.1 Droplet theoretical and experimental data without imposed vibrations on teflon surface	51
Table 5.2 Droplet theoretical and experimental data without imposed vibrations on copper surface	51
Table 5.3 Droplet theoretical and experimental data without imposed vibrations on aluminum surface.....	51
Table 5.4 Calculated resonance frequencies for different droplet volumes and different surfaces	53
Table 5.5 Experimental resonance frequencies for different droplet volumes and different surfaces	55
Table 5.6 Acoustic model and experimental data for the first resonance mode on teflon surface	60
Table 5.7 Acoustic model and experimental data for the first resonance mode on copper surface	60
Table 5.8 Acoustic model and experimental data for the first resonance mode on aluminum surface.....	60
Table 5.9 Acoustic model and experimental data for the second resonance mode on teflon surface	60
Table 5.10 Acoustic model and experimental data for the second resonance mode on copper surface	61
Table 5.11 Acoustic model and experimental data for the second resonance mode on aluminum surface.....	61
Table 5.12 Sliding angle enhancement using a teflon surface	63
Table 5.13 Sliding angle enhancement using a copper surface.....	63
Table 5.14 Sliding angle enhancement using an aluminum surface	63

Table 5.15 Droplet size distribution at an average surface temperature of 2.6 °C (Note ¹ : volume and other calculations can be found in Appendix A).....	66
Table 5.16 Condensation results using a copper surface without imposing acoustic vibrations	69
Table 5.17 Condensation results using an aluminum surface without imposing acoustic vibrations	69
Table 5.18 Condensation results using a hydro-copper surface without imposing acoustic vibrations	70
Table 5.19 Condensation results using a painted metallic surface without imposing acoustic vibrations	70
Table 5.20 The simple oscillator expression to obtain the rocking mode excitation, ω_0 , values.....	73
Table 5.21 Condensation results using a copper surface while imposing acoustic vibrations	74
Table 5.22 Condensation results using an aluminum surface while imposing acoustic vibrations	75
Table 5.23 Condensation results using a hydro-copper surface while imposing acoustic vibrations	75
Table 5.24 Condensation results using a painted metallic surface while imposing acoustic vibrations	75
Table A.1 Physical properties of liquid droplets.....	97
Table A.2 Condensed droplet characteristics based on droplet contact radius, contact area, height, and surface area on the fluid side.....	99
Table A.3 Droplet theoretical and experimental data without imposed vibrations on SiO ₂ surface	100
Table A.4 Acoustic model and experimental data for the first resonance mode on SiO ₂ surface.....	100
Table A.5 Acoustic model and experimental data for the second resonance mode on SiO ₂ surface	100

1. INTRODUCTION

1.1 Motivation

In condensation, it has been found that dropwise condensation promotes higher rates of heat transfer than film-wise condensation [1-3]. During dropwise condensation, each droplet nucleates, grows, coalesces, and sheds depending on their sizes and history. However, poor droplet shedding still hinders the whole condensation process since it limits the availability of nucleation sites over time. In recent studies, engineered surfaces have been used to increase the contact angles of droplets while decreasing contact angle hysteresis to facilitate droplet shedding and enhanced condensation heat transfer [4]. Also, it has been shown that hydrophobic surfaces consisting of hydrophilic sites can promote faster nucleation rates, but with limited shedding ability, which could lead to film-wise condensation [5]. Moreover, most engineered surfaces cannot last under the conditions found in condensers. Therefore, an alternative way of promoting droplet shedding should be explored.

Recently, it has been validated that imposing low energy, low frequency acoustic vibrations enable droplet mobility [5-7]. Furthermore, a recent study has shown that mechanical vibrations can enable better heat transfer rate [8, 9]. However, the exact mechanisms that enhance droplet shedding under the effects acoustic stimuli still need to be understood at the most fundamental level. The research aims to uncover the physical mechanisms that would enable greater droplet shedding ability and enhanced dropwise condensation under the effects of resonant low frequency acoustics. Future studies

should emphasize in a development of a physics-based model that accounts for the effects of multi-mode acoustic streaming spectra on dropwise condensation.

Furthermore, the use of hydrophobic surfaces with patterned hydrophilic sites for enhanced droplet nucleation under the effects of multi-modal resonance spectra may be evaluated in terms of condensation efficiency. Multi-resonance vibration modes should facilitate droplet shedding in condensation systems, which should result in enhanced condensation heat transfer performance, when using standard surfaces.

1.2 Objectives

The main objective of the study is to understand the interplay between acoustic stimuli and droplet shedding during dropwise condensation, from the theoretical and experimental perspectives; when using standard surfaces. A study of the effects of induced vibrational modes on droplet sliding has been explored analytical and experimentally to enable lower sliding angles. Lai [6] studied the effects of droplet sliding-off angles while imposing low-energy, low frequency acoustic vibrations. Her experimental results revealed that resonance modes of vibrations help indeed reduce droplet-sliding angles. However, the study did not include the development of a governing equation capable of estimating sliding angle. Recently, a mathematical physics-based model has been developed, which can predict droplet-sliding angles while using a variety of surfaces including those with hydrophobic and hydrophilic wetting characteristics. The model is capable of estimating sliding angles of droplets with and without acoustic vibrations on the surface.

The development of the model was based on Noblin *et al.* [10], who developed a model capable of estimating resonance frequencies based on the droplet contact angle and contact line, and other droplet-surface properties. The Noblin's model was used initially to calculate theoretical resonance frequency values necessary to induce resonant vibrations on each droplet-surface combination. The Noblin's model was incorporated into the droplet-sliding model to obtain the amplitude acceleration when using an acoustic sensor, a condensation cell and a data acquisition system.

In summary, the overall objectives of the research are to uncover the physical mechanisms that would enable droplet shedding ability under the influence of acoustic streaming. A governing equation has been formulated to predict droplet-sliding angle by considering droplet-surface properties. Sliding angle data under the effects of resonance acoustics were obtained using a customized experimental setup, which was used to validate the analytical model. Moreover, a customized acoustic system was coupled with a condensation cell to determine the effects of low frequency acoustics on dropwise condensation in terms of heat flux enhancement. Empirical correlations for dropwise condensation under the effects of acoustic streaming on hydrophilic and hydrophobic surfaces have been postulated and validated experimentally.

2. BACKGROUND AND LITERATURE REVIEW

Recent studies have been performed to enhance the dropwise condensation with different wetting surface characteristics analytically and experimentally. Most of the recent studies in the area of condensation focuses on hybrid surfaces, where engineered surfaces have been fabricated with different nano-structure characteristics to enhance wetting properties and condensation rate. However, little focus has been given to the use of external mechanisms or stimuli to promote dropwise condensation. In such cases, droplets on the surfaces should shed before transitioning to film-wise condensation since it is characterized by depicting lower heat transfer rates. Therefore, an acoustic stimuli approach should be developed to facilitate droplet shedding for the early stages of condensation. In this chapter, a review of studies related to fundamental theory of droplet wetting characteristics, surface morphology and dropwise condensation is presented.

2.1 Fundamental theory of droplet sliding model

Surface properties from liquid/solid combinations are the most important factors to describe the retention force of droplets on solid surfaces. The wetting characteristics of droplets have been examined in previous investigations to predict analytically the retention force of liquid droplets [11]. Furnidge [12] predicted a retention force factor for liquid droplet on a solid surface, as follows:

$$F = \theta_M \left[\frac{\gamma_{AL} (\cos \theta_R - \cos \theta_A)}{\rho} \right]^{\frac{1}{2}} \quad (1)$$

where θ_A , θ_R , θ_M , γ_{AL} , and ρ are the advancing contact angle, receding contact angle, the arithmetic means of advancing and receding angle, the air/liquid surface tension and density of the liquid. To predict the retention force acting on the droplet, several factors, including contact angle and surface tension should be considered.

2.1.1 Contact angles on distinctive surface wetting properties

Studies have shown that the droplet's contact angle varies depending on the morphology of the surface [13-15]. Contact angles are related to liquid surface tensions and they can be calculated from liquid droplets placed horizontally on distinctive surface-property combinations. Contact angles can be related to the Young's equation [13-15], which takes into account surface tension forces between distinct phases (liquid/gas, solid/gas, solid/liquid), as follows:

$$\gamma_{LG} \cos \theta = \gamma_{SG} - \gamma_{SL} \quad (2)$$

Fig. 2.1 shows the relationship between the surface tension components for two cases. When the contact angle θ is lower than 90° , the surface is considered hydrophilic, and if the contact angle θ is higher than 90° , the surface depicts hydrophobic characteristics.

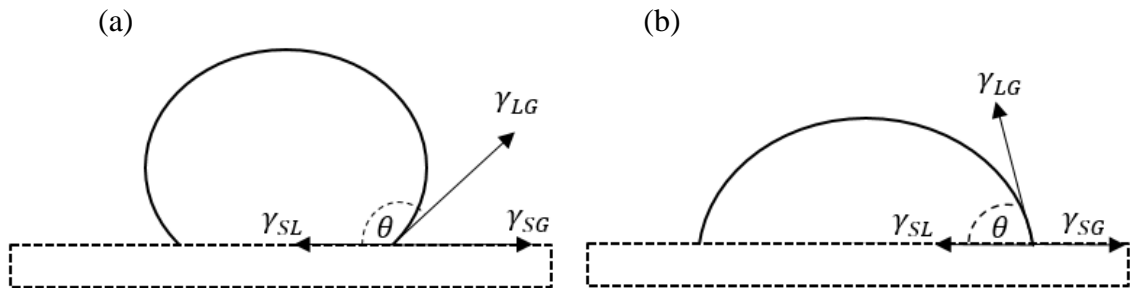


Fig. 2.1 Surface tension components and contact angle of a droplet on (a) hydrophobic surface, (b) hydrophilic surface

Engineered surfaces, those with hydrophobic and hydrophilic combined characteristics, have been studied by several researchers [16] and have been determined that they do not last over an extended period of time. Although such surfaces facilitate droplet shedding due to their hydrophobic characteristics, investigations with hybrid surfaces usually involved the pinning effect, which is detrimental to droplet shedding. Most of the typical studies with hybrid surfaces considered the Wenzel and Cassie-Baxter cases, where surfaces are manufactured with nano-structured pillar-to-pillar hydrophilic and hydrophobic properties [15-17].

Many researchers have continued to develop such surfaces, with distinct wetting properties and have studied the relationship between surface energy and contact angle hysteresis from different perspectives. As shown in Fig 2.2, the Cassie-Baxter state depicts higher contact angle compared to the Wenzel state as the droplet fall within the hydrophilic-wetting properties region. In most cases, studies focus on the surface energy based on the modified Young's contact angle as follows [16]:

$$E = \gamma_{LG} [A_{LG} - \cos \theta_0 A_p] \quad (3)$$

where A_p is the projected base area and θ_0 is the contact angle. Hence, the surface energy based on all wetting conditions is given by:

$$E = \gamma_{LG} \left[A_{LG} - A_p \left([r_f f_w + \phi(1 - f_w)] \cos \theta_0 - (1 - f_w)(1 - \phi) \right) \right] \quad (4)$$

Due to a variety of existing nano-structured surfaces manufactured, many researchers have modified the Young's equation to take into account the homogeneous and

heterogeneous wetting characteristics of engineered surfaces [16]. Due to the pinning effect that occurs on hybrid surfaces, they are not considered in this study.

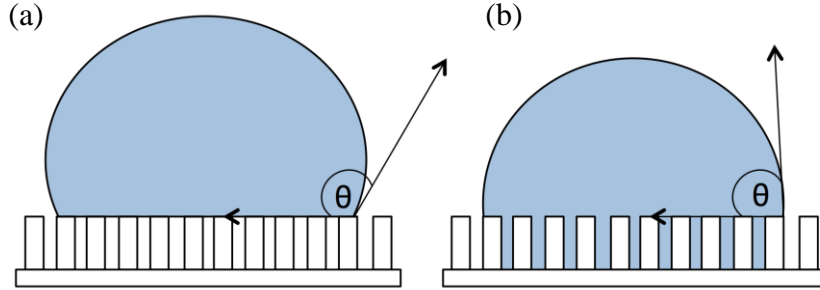


Fig. 2.2 Droplet with different wetting characteristics of (a) Cassie-Baxter condition and (b) Wenzel condition

2.1.2 Contact angle hysteresis effect

Hysteresis can be defined as an activated energy barrier that prevents any droplet dynamic behavior on an interfacial area to occur [18-19]. When a droplet is placed on an inclined surface, an external force (i.e. gravity) acts upon the droplet, which it may overcome the energy barrier caused by the hysteresis effect. The droplet deforms and starts sliding off the surface, where the advancing angle (θ_A) of the droplet becomes larger than the receding angle (θ_B) as shown in Fig. 2.3. Therefore, the equilibrium contact angle changes and the difference between the advancing and receding angle is called the contact angle hysteresis [20]. The contact angle hysteresis (CAH) is the most fundamental concept for droplet shedding and is mathematically defined as

$$\Delta\theta = \theta_A - \theta_R \quad (5)$$

Moreover, sliding on droplets happens only if it overcomes the energy barrier caused by the hysteresis effect and it can easily be achieved by motion of liquid drops [21-22].

Experimentally, the contact angle hysteresis may be determined from droplet static images and image-processing software [23].

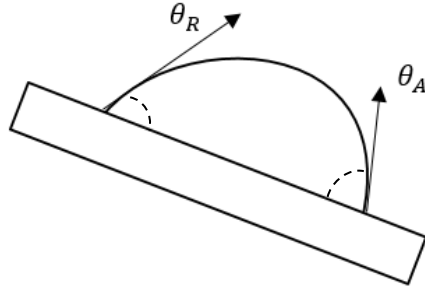


Fig. 2.3 Depiction of contact angle hysteresis

2.1.3 Relation between contact angles, drop shape, retention force, and sliding

Several investigations had been overtaken to formulate the volume of a semi-spherical droplet with different surface-property characteristics. It has been seen that for very small contact angle hysteresis, the curvature of the droplet, with nearly a circular contact line, forms into a semi-spherical cap [24]. Methodologically, the volume of the droplet can be expressed as follows:

$$\Omega = \frac{\pi}{3} R^3 (2 + \cos \theta)(1 - \cos \theta)^2 \quad (6)$$

The equation shows that knowing the volume and diameter of the droplet, contact angle can be directly determined from Equation 6.

Sliding angle of droplets on inclined surfaces have been studied for decades [25-26]. For the droplet to move, the droplet must overcome the energy barrier caused by the

hysteresis effect. It has been postulated that, due to the hysteresis effect, a droplet that remain at rest on a tilted plane [24] can be expressed as follows:

$$\pi r \gamma (\cos \theta_r - \cos \theta_a) \geq \rho \Omega g \sin \alpha \quad (7)$$

where r is the radius contact line ($r = R \sin \theta$) of the droplet, ρ , γ and g are the density of the liquid, surface tension and gravitational acceleration. Therefore, for a steady droplet, the capillary length of the droplet ($\kappa^{-1} = \left(\frac{\gamma}{\rho g}\right)^{\frac{1}{2}}$) should be larger than the droplet size.

A retention force occurs when a liquid droplet resting on a surface start moving at an inclined stage. If receding angle is greater than zero, e.g. $\theta_r > 0$, and the force exceeds the critical value, the droplet starts sliding-off the surface. The retention force is related to advancing and receding angles and it has been modeled as follows [27-28]:

$$\frac{F}{\gamma} R = k (\cos \theta_r - \cos \theta_a) \quad (8)$$

The shape of the droplet, k , may vary depending on the droplet length and shape. It has been investigated that for a circular contact line, the shape factor k can be predicted as $4/\pi$ [29]. For parallel-side droplets, based on Dussan V. and Chow experiments [30], for highly elongated droplets, with constant receding and advancing angles, the shape factor can be predicted as $k = 2$. However, Extrand *et al.* [27] derived an equation to estimate the shape factor regardless of droplet elongation as follows:

$$k = -\frac{2}{\pi} \int_0^\pi \phi \cos \phi [\beta^2 \cos^2 \phi + \sin^2 \phi]^{\frac{1}{2}} d\phi \quad (9)$$

where β is the length-to-width aspect ratio and ϕ is the angle between the droplet contact line and radius. Numerically, as k increases with droplet elongation, the following correlation can be applied as [27]:

$$k = 0.23 + 1.04\beta \quad (10)$$

where β is the aspect ratio of the contact line in length and width, then $\beta = \frac{L}{w}$ as shown in Fig. 2.4.

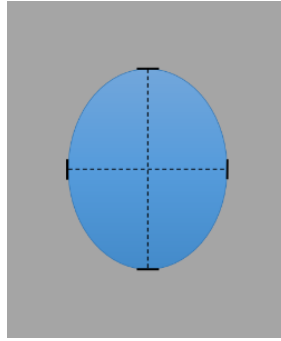


Fig. 2.4 Plane view of liquid droplets with most common shape at an inclined plane

2.2 Vibrations of liquid droplets

An acoustically vibrational stimulus has been considered as an effective way to promote droplet motion on surfaces. The following section discusses studies that were previously performed to understand the influence of using resonance-induced acoustics for droplets motion to help overcome the hysteresis effect.

2.2.1 Contact line oscillation modes

Oscillations and inertial contact line dynamics of spherical liquid droplets have been studied for more than a century. The resonance of droplet oscillations can be

described by the frequency induced where the maximum peak occurs [31]. Previously, Lamb [32] formulated an expression that determines the resonant frequency with different modes of vibrations as follows:

$$f_r = \sqrt{l(l-1)(l-2) \frac{\sigma}{3\rho\pi V}} \quad (11)$$

where f_r is the resonance mode frequency, l is the mode number, V is the droplet volume, σ is the surface energy and ρ is the liquid density. However, droplet characteristics, such as droplet contact line and droplet contact angle are not considered in the Lamb equation. Therefore, the equation does not account for the sessile drop vibration adequately with respect to surface-property characteristics.

A recent study on vibrated sessile drops on wetting properties [10] focused on the determination of a model that predicts the resonance frequencies for a fixed contact line (known as the Type-I modes) and a fixed contact angle with free contact line (known as the Type-II modes). Immobile contact line (Type I) is characterized with low amplitude acceleration, as follows:

$$a = -(2\pi f)^2 u_0 \cos(2\pi f t) \quad (12)$$

where u_0 is the displacement of the substrate. For a liquid droplet, at Type-I mode, the contact line remains pinned and the contact angle oscillates within time [10]. However, as for Type-II mode, while yielding higher amplitudes, the vibrations imposed to the substrate overcome the energy barrier from the hysteresis effect [33-35], which leads to motion of the contact line of the droplet [10].

2.2.2 Prediction of resonant modes of vibrations in droplets

The prediction of resonant modes of vertical vibrations have been undertaken by Noblin. [10] by taking into account different surface-wetting characteristics. Noblin performed investigations on the effects of vertical vibrations on droplets and proposed a model that considers both droplet contact and contact line as shown in Fig. 2.5.

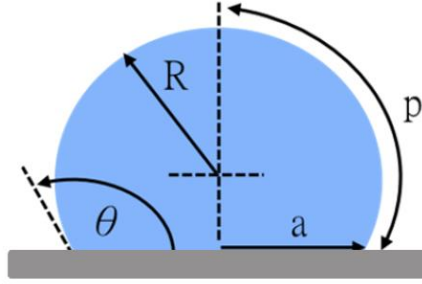


Fig. 2.5 Droplet contact schematic illustrating droplet contact angle and contact line

Based on immobile contact line Type-I mode, the proposed model for vertical resonance frequency ω_j was postulated as follows [10]:

$$\omega_j^2 = \left(g q_j + \frac{\gamma}{\rho} q_j^3 \right) \tanh \left(\frac{q_j V}{\pi a^2} \right) \quad (13)$$

where j is the resonance mode number, q_j is the wave factor (1-D capillary-gravity wave), a is the drop contact radius ($a = R \sin \theta$), and p is the half arc length of the droplet. The q_j is defined as:

$$q_j = \frac{\pi(j - 0.5)}{p} \quad (14)$$

For sessile droplets, p is based as a function of volume and it was calculated based on experimental results. Moreover, an expression for the half arc length of the droplets has been developed as follows [36]:

$$p = R\theta \quad (15)$$

and based to Quéré [24], the droplet radius can be obtained based on contact angle and droplet volume:

$$R = \left(\frac{3V}{\pi(1 - \cos \theta)^2(2 + \cos \theta)} \right)^{\frac{1}{3}} \quad (16)$$

The vibrational model help identify the corresponding frequency for each droplet-surface combination as droplet excites through resonance. To overcome the energy barrier from contact angle hysteresis, several types of imposed frequencies should be considered to determine the highest lateral motion of the liquid droplet. The Noblin's model can be used to determine the greatest level of lateral motion for each droplet-surface combination. Noblin [10] characterized different vibrational modes in his model, where it consists of a superposition of eigen-modes. It has been observed that droplet excite the highest when the number of nodes along the drop profile increases. While inducing vibration to the substrate, drop profile varies depending on the resonance mode imposed. Fig 2.6 shows that imposing the first and second resonance modes, 2 and 4 nodes can be observed, respectively [10].

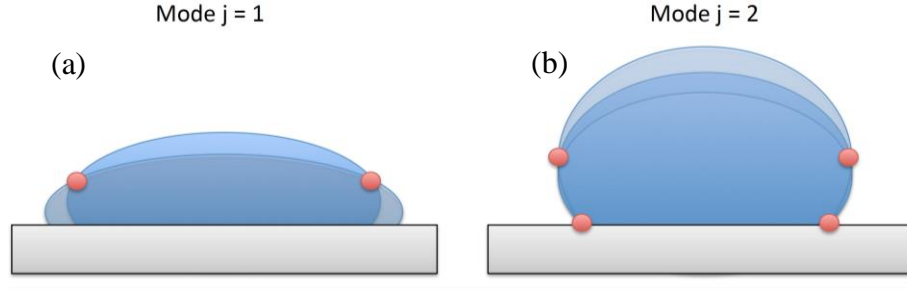


Fig. 2.6 Droplet schematic depicting modes of vibrations of mode (a) $j=1$ (2 nodes) and (b) $j=2$ (4 nodes).

A recent study by Celestini and Kofman [37] reveals that a simple oscillator model is capable of estimating the vibration mode of submillimeter-size droplets. The semi-analytical expression for eigenfrequencies for droplet and energy dissipation was developed, as follows:

$$\omega_0 = \sqrt{\frac{6\gamma h(\theta)}{\rho(1 - \cos \theta)(2 + \cos \theta)}} R^{-\frac{3}{2}} \quad (17)$$

where $h(\theta)$ is numerically computed and is dependent on wetting contact angle, θ . $h(\theta)$ is based on the assumption that the deformations of droplets are a direct result of surface energy minimization under the influence of an external force. Based on vibration studies [10, 37], the calculated frequency values accurately agree with the experimental results. Despite recent studies that considered the use of acoustics on droplet morphology, very few studies have been undertaken to understand the role of low frequency acoustics on droplet mobility.

2.3 Condensation heat transfer

The study of dropwise condensation has been investigated over the past century. New surfaces have been designed and fabricated to enhance and promote dropwise condensation heat transfer. In addition, the heat transfer coefficient for dropwise condensation is about an order of magnitude greater than those of film-wise condensation. It has been shown that in order to maintain dropwise condensation, it is desired that the surface should exhibit strong wetting characteristics (i.e. hydrophobic characteristics). In this section, a brief review of studies regarding to dropwise condensation is presented.

2.3.1 Dropwise condensation

In the process of condensation, condensation occurs when the vapor's temperature is below the saturated temperature. Several investigations in condensation heat transfer have been undertaken over the years. Schmidt *et al.* [1] investigated the process of the condensation heat transfer on surfaces. As the surface condenses, discrete droplets at the surface nucleate, grow, coalesce, and shed away from the surface. There are two types of modes of condensation, film-wise and dropwise. In film-wise, a condensate thin-film covers the surface whereas in dropwise, gravitational forces overcome the capillary forces where droplets do not coalesce and slides off the surface.

Rose [3] proposed an analytical approach to predict dropwise condensation under certain conditions. They also concluded that a higher order of magnitude in heat transfer coefficient can be achieved in dropwise condensation than in film-wise mode. However, even in dropwise condensation droplet tends to grow up to a maximum size, which

frequently lead to film-wise after droplet coalescence. Therefore, a reduction in droplet size and greater droplet departure rate has been studied since it promotes higher rates of heat transfer per contact area [38], specifically before the onset of droplet coalescence. Investigations have proposed that surfaces with hydrophobicity properties reveal faster droplet shedding, resulting in enhanced heat transfer [39].

To facilitate droplet shedding, mechanical vibrational systems have been manufactured to prevent large droplet growth and to enable greater heat transfer rate [9, 40]. It is also known that the number of droplets on a surface affect condensation. Le Fevre and Rose [9, 41] derived a drop size distribution equation to evaluate the effect of condensation droplets as follows,

$$N(r) = \frac{1}{3\pi r^2 r_{\max}} \left(\frac{r}{r_{\max}} \right)^{-\frac{2}{3}} \quad (18)$$

Recently, a study by Migliaccio [9] has shown that lower frequencies and imposed vibrations enable better heat transfer during dropwise condensation. Furthermore, imposed mechanical vibrations on surfaces limit the size and number of large droplets, which leads to improvements in energy efficiency and performance.

2.4 Conclusion

Previous studies demonstrate that while imposing resonant vibrations, contact angle hysteresis may be overcome. However, an analytical model has not been proposed or validated, which could be used to determine the sliding-off angle of droplets on sliding surfaces. Furthermore, an acoustic system should be developed to facilitate droplet shedding and hence improve the overall condensation heat transfer performance by taking advantage of the droplets' resonant frequencies and vibrational mode.

3. DEVELOPMENT OF PHYSICS BASED MATHEMATICAL MODEL FOR DROPLET SLIDING

An important consideration in the study of dropwise condensation, it is the ability of droplets to slide on hydrophobic and hydrophilic surfaces. The following two subsections shows how physics-based models were developed to estimate sliding angle with and without the effects of imposed resonant frequencies. Therefore, the postulated model was validated using droplet sliding angles and droplet volumes through a customized experimental setup.

3.1 Formulation of droplet sliding-off angle without imposing acoustics

The governing equation for the sliding droplet model is based on the balance of forces acting on the droplet at the moment it starts sliding off the surface. The applied forces on the droplet consist of capillary and gravitational forces, and vibrational forces (when vibrations are imposed). The sum of forces equation ($\sum F = 0$) under consideration (without and with vibrational force) are as follows:

$$F_{\text{cap}} + F_g = 0 \quad (19)$$

$$F_{\text{cap}} + F_g + F_v = 0 \quad (20)$$

where F_{cap} is the capillary force, F_g is the gravitational force, and F_v is the vibrational force, as shown in Fig. 3.1. One important consideration in the development of a droplet sliding angle model is the effect of viscous forces on droplet sliding. To understand the potential effect of viscous forces, the viscous force (dissipation) to surface tension force ratio or Capillary number (Ca) should be determined. The Ca number is as follows:

$$Ca = \frac{\mu v}{\gamma} \ll 1 \quad (21)$$

If the capillary number, Ca , is much less than one, the surface tension effects are more dominant than viscous forces (i.e. friction force), see Appendix A for more details. As shown in Appendix A, neither the macroscopic flow or pinning-depinning friction mechanism within each droplet is significant enough to counteract the effects of surface tension and body forces (i.e. gravity) on droplet sliding. Therefore, F_{vis} is considered to be negligible and not taken into account in the governing equation.

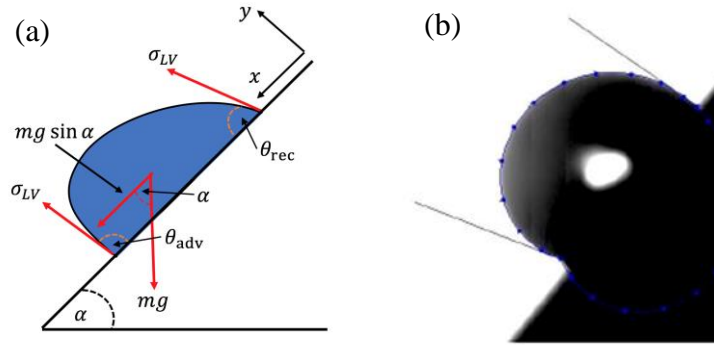


Fig. 3.1 (a) Tilted surface at a specific droplet sliding angle α ; advancing and receding angle, and (b) experimental droplet sliding

In the process of developing the mathematical model to estimate accurately the sliding angle of a droplet on an inclined plane without the vibrational force (Equation 19), the following equation has been considered, as follows:

$$mg \sin \alpha = kr\gamma_{LG}(\cos \theta_r - \cos \theta_a) \quad (22)$$

where $F_g = -mg \sin \alpha$, $F_{\text{cap}} = kr\gamma_{LG}(\cos \theta_r - \cos \theta_a)$, γ_{LG} is the surface tension, θ_r is the receding angle, θ_a is the advancing angle, m is the mass of the droplet, g is the gravitational acceleration, and α is the sliding angle. The droplet contact radius (r) is used to estimate F_{cap} , and it is defined as $r = R \sin \theta$. The shape factor, k , is the dimensionless factor that accounts for the aspect ratio for a droplet with non-spherical shape during sliding [27]. The k value varies depending on the droplet length and shape, and it can be obtained from using Equation 10. Hence, the governing Equation 23 is solved for sliding angle, α , as follows:

$$\cos \theta_r - \cos \theta_a = \frac{\rho V g}{kr\gamma_{LG}} \sin \alpha \rightarrow \sin \alpha = \frac{kr\gamma_{LG}}{\rho V g} (\cos \theta_r - \cos \theta_a) \quad (23)$$

According to Quéré [24], the volume of the droplet can be expressed as follows:

$$\Omega = \frac{\pi}{3} R^3 (2 + \cos \theta)(1 - \cos \theta)^2 \quad (24)$$

In the following expression, Ω is expressed as V , which is inserted to Equation 23, as follows:

$$\cos \theta_r - \cos \theta_a = \frac{1}{kR \sin \theta \gamma_{LG}} \left[\rho g \sin \alpha \frac{\pi}{3} R^3 (2 + \cos \theta)(1 - \cos \theta)^2 \right] \quad (25)$$

where $r = R \sin \theta$. By simplifying Equation 25, the following equation is obtained:

$$\cos \theta_r - \cos \theta_a = \frac{\pi}{3k} \cdot \frac{\rho g}{\gamma_{LG}} \cdot R^2 \cdot \frac{(2 + \cos \theta)(1 - \cos \theta)^2}{\sin \theta} \cdot \sin \alpha \quad (26)$$

It has been defined that the contact angle hysteresis of a sliding droplet is $\Delta\theta = \theta_a - \theta_r$.

Moreover, as a droplet is placed on an inclined plane, the advancing angle of the droplet becomes larger than the receding angle, and it can be estimated using the following relationships:

$$\theta_r = \theta - \frac{\Delta\theta}{2} \quad (27)$$

$$\theta_a = \theta + \frac{\Delta\theta}{2} \quad (28)$$

From trigonometry identities and using the “sum-to-product” rule, the following expression from the left-hand side of Equation 26 is obtained as follows:

$$\cos\left(\theta - \frac{\Delta\theta}{2}\right) - \cos\left(\theta + \frac{\Delta\theta}{2}\right) = 2 \sin \theta \sin\left(\frac{\Delta\theta}{2}\right) \quad (29)$$

If $\frac{\Delta\theta}{2} \ll 1$, then $\sin\frac{\Delta\theta}{2} \approx \frac{\Delta\theta}{2}$, (e.g. $\Delta\theta \approx 10^\circ \approx 0.17$ rad and $\Delta\theta \approx 20^\circ \approx 0.34$ rad.)

Therefore, Equation 26 can be simplified as follows:

$$\sin \theta \cdot \Delta\theta = \frac{\pi}{3k} \cdot \frac{\rho g}{\gamma_{LG}} \cdot R^2 \cdot \frac{(2 + \cos \theta)(1 - \cos \theta)^2}{\sin \theta} \cdot \sin \alpha \quad (30)$$

Solving for α ,

$$\alpha = \sin^{-1} \left[\frac{3k}{\pi} \cdot \frac{\gamma_{LG}}{\rho g} \cdot \sin^2 \theta \cdot \Delta\theta \cdot \frac{1}{R^2} \cdot \frac{1}{(2 + \cos \theta)(1 - \cos \theta)^2} \right] \quad (31)$$

By considering the following assumption,

$$\sin \frac{\Delta\theta}{2} \approx \frac{\Delta\theta}{2} \quad (32)$$

Equation 31 can be transformed as follows:

$$\alpha = \sin^{-1} \left[\frac{6k}{\pi} \cdot \frac{\gamma_{LG}}{\rho g} \cdot \sin^2 \theta \cdot \sin\left(\frac{\Delta\theta}{2}\right) \cdot \frac{1}{R^2} \cdot \frac{1}{(2 + \cos \theta)(1 - \cos \theta)^2} \right] \quad (33)$$

where $k = 0.23 + 1.04\beta$, and $\beta = \frac{L}{w}$ is the aspect ratio of the droplet in terms of length and width measurements. In summary, Equation 33 can be used to estimate sliding angle accurately without the effects of imposed vibrations.

3.2 Formulation of droplet sliding-off angle under the effects of imposed resonant acoustic frequencies

To estimate the sliding angle under the effects of resonant vibrational excitations, a maximum vibrational force should be taken into account in the sum of forces equation. Therefore, the balance of forces when taking vibrational forces is as follows:

$$kr\gamma_{LG}(\cos \theta_r - \cos \theta_a) - mg \sin \alpha - \rho V a_0 = 0 \quad (34)$$

where a_0 is the acceleration or amplitude of the vibration excitation along the downward sliding direction. The sum of forces equation is based on the assumption that static contact angle data is sufficient to estimate sliding angle even under the effects of dynamic oscillations of droplets. The acceleration or amplitude of the acoustic oscillation is measured experimentally.

To determine the sliding angle of droplets under the effects of imposed acoustics, Equation 34 is transformed as follows:

$$\cos \theta_r - \cos \theta_a = \frac{\rho V g \sin \alpha + \rho V a_0}{kr\gamma_{LG}} \quad (35)$$

Substitute $r = R \sin \theta$ and $V = \frac{\pi}{3} R^3 (2 + \cos \theta)(1 - \cos \theta)^2$, then

$$\cos \theta_r - \cos \theta_a = \frac{1}{k\gamma_{LG} R \sin \theta} \left[\left(\frac{\pi}{3} R^3 \rho \right) (g \sin \alpha + a_0) ((2 + \cos \theta)(1 - \cos \theta)^2) \right] \quad (36)$$

Previously, it has been defined that $\theta_r = \theta - \frac{\Delta\theta}{2}$ and $\theta_a = \theta + \frac{\Delta\theta}{2}$. Then, using trigonometry identities on the left-hand of Equation 36, the following expression is obtained:

$$\cos \left(\theta - \frac{\Delta\theta}{2} \right) - \cos \left(\theta + \frac{\Delta\theta}{2} \right) = 2 \sin \theta \sin \left(\frac{\Delta\theta}{2} \right) \quad (37)$$

Hence, (from previous derivation, e.g. Equation 30,)

$$\sin \theta \cdot \Delta\theta = \frac{1}{k\gamma_{LG}R \sin \theta} \left[\frac{\pi}{3} R^3 (2 + \cos \theta)(1 - \cos \theta)^2 \right] [\rho g \sin \alpha + \rho a_0] \quad (38)$$

And solving for α ,

$$\alpha = \sin^{-1} \left[\frac{3k}{\pi} \cdot \frac{\gamma_{LG}}{\rho g} \cdot \sin^2 \theta \cdot \Delta\theta \cdot \frac{1}{R^2} \cdot \frac{1}{(2 + \cos \theta)(1 - \cos \theta)^2} - \frac{a_0}{g} \right] \quad (39)$$

Assuming that $\sin\left(\frac{\Delta\theta}{2}\right) \approx \frac{\Delta\theta}{2}$ for low contact angle hysteresis, the following expression for estimating the sliding angle of the droplet while imposing vibrations to the droplet is as follows:

$$\alpha = \sin^{-1} \left[\frac{6k}{\pi} \cdot \frac{\gamma_{LG}}{\rho g} \cdot \sin^2 \theta \cdot \sin\left(\frac{\Delta\theta}{2}\right) \cdot \frac{1}{R^2} \cdot \frac{1}{(2 + \cos \theta)(1 - \cos \theta)^2} - \frac{a_0}{g} \right] \quad (40)$$

The derived expressions have been validated using droplet sliding angles, droplet volumes, excitation frequencies through experimentation, as shown in the Results and Discussion chapter.

4. EXPERIMENTAL SETUP AND PROCEDURE

To accomplish the goals of this research project, an experimental set-up was developed to conduct droplet-sliding observations. The set-up was used to validate the developed physics-based mathematical model described in Chapter 3. The induced acoustic vibrational system used for droplet shedding experiments consist of a high-speed camera (Photron SA3,) amplifier, data acquisition system, speaker, acoustic sensor, backlight illumination, computer and tilting stage system as shown in Fig. 4.1 and Fig. 4.2.

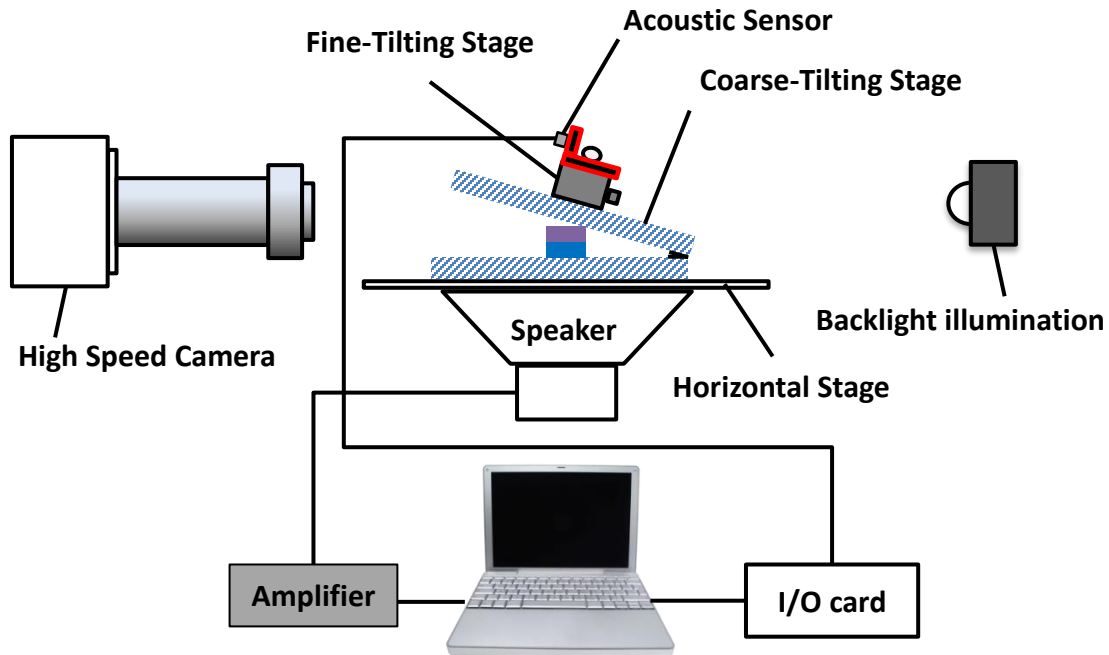


Fig. 4.1 Experimental setup to validate the developed sliding models [6]

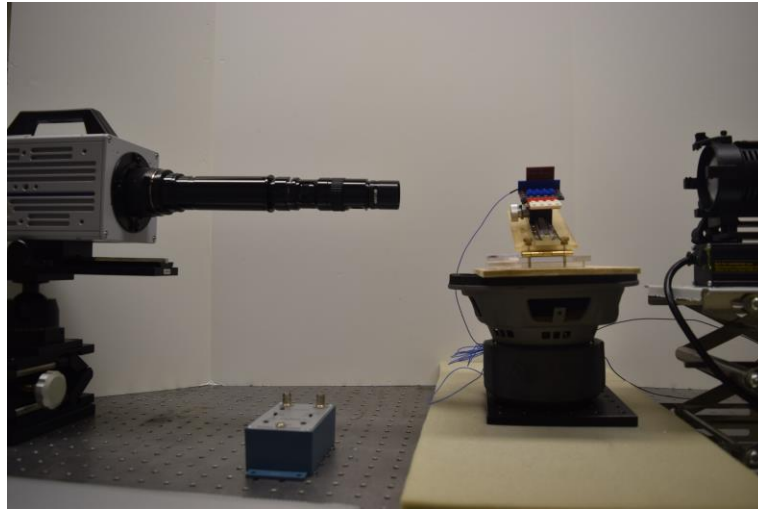


Fig. 4.2 Experimental setup for droplet sliding

Experiments were performed at a room temperature (21 – 22 °C) on top of an optical table to prevent any additional noise coming to the system that could alter the frequency and amplitude measurements. A piece of foam was placed underneath the speaker to absorb any additional vibrations coming from the optical table. Each component of the experimental set up is described below.

4.1 Tilting stage system for droplet sliding

In the study of droplet shedding, a customized coarse tilting stage system has been developed to perform droplet sliding-off angle experimentally, as shown in Fig. 4.3. An external L-shape Lego piece was designed to place an accelerometer (Model 1000A) along the sliding plane for precise amplitude measurements. It was used to determine the imposed acceleration or acoustic amplitude as shown in Equation 40.

$$\alpha = \sin^{-1} \left[\frac{6k}{\pi} \cdot \frac{\gamma_{LG}}{\rho g} \cdot \sin^2 \theta \cdot \sin \left(\frac{\Delta\theta}{2} \right) \cdot \frac{1}{R^2} \cdot \frac{1}{(2 + \cos \theta)(1 - \cos \theta)^2} - \frac{a_0}{g} \right] \quad (40)$$

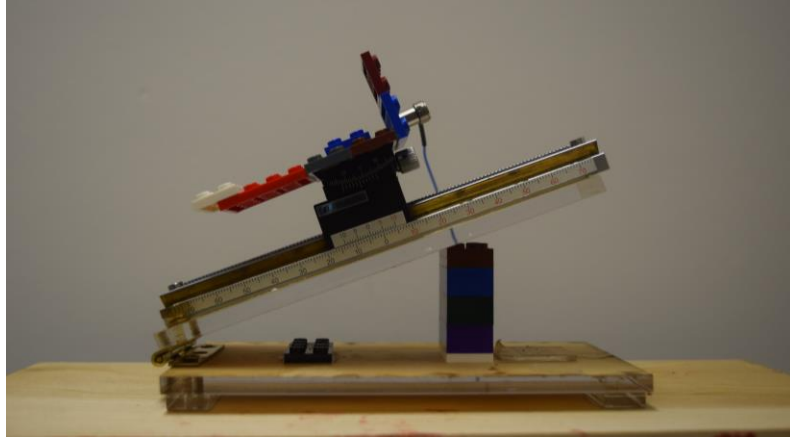


Fig. 4.3 Tilted stage system utilized to perform droplet sliding experiments

The coarse tilting stage system can be adjusted using a goniometer (OptoSigma Inc.) as a fine-tilting stage which provides a maximum tilting angle stage difference of $\pm 15^\circ$. Lego blocks were used to obtain steeper inclination angles in addition to the fine-tilting stage ($\pm 15^\circ$). Examples of inclination angles are shown in Fig. 4.4. The inclination angles were measured by taking photographic images, which were processed using an image processing software (imageJ).

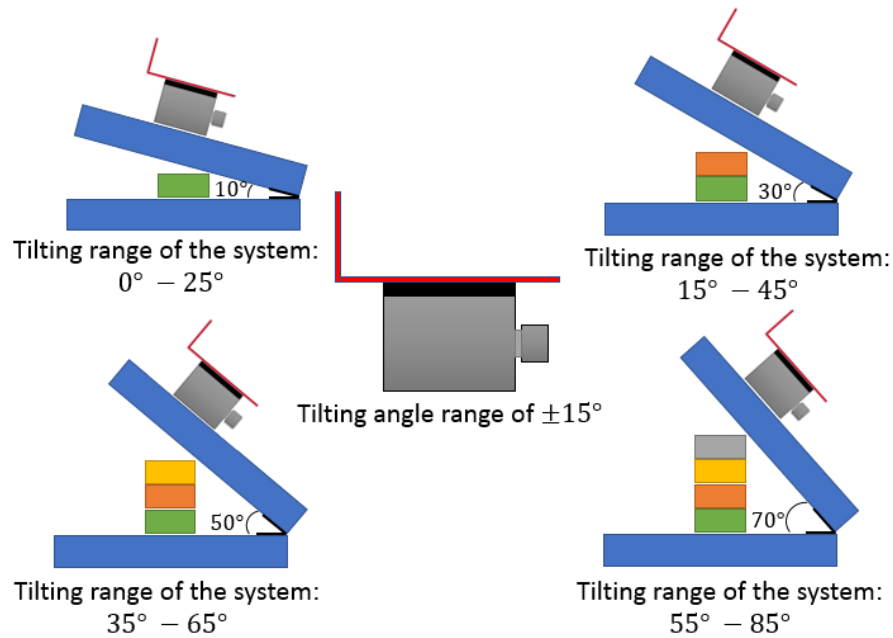


Fig. 4.4 Schematic of tilting range systems

4.2 Vibrational system for droplet sliding

An Infinity Reference 860w (Infinity Inc.) sound speaker was utilized to impose vertical vibrations on the system to enhance droplet shedding as shown in Fig. 4.5. The speaker was attached to a Russound P75 2-Channel Dual Source 75w amplifier system. The amplifier system was used to impose vibrations to the system through the speaker. The frequency response of the speaker was adjusted from a minimum of 20 Hz to a maximum of 100 Hz for all vibration experiments. The same sound system (speaker and amplifier) was used to impose acoustic signals to a condensation system as discussed below. A tone generator software (NHC Inc.) was utilized to impose and control specific frequencies from the speaker to the system.



Fig. 4.5 Infinity Reference 860w that was utilized to impose vibrations to the system

4.3 Data acquisition system (DAQ board)

An accelerometer (Model 1000A) with a power supply (P5000, MISTRAS group Inc.) was used as a sensor to measure the resonant frequencies and amplitudes or accelerations during all vibration experiments. The acoustic sensor was attached along the sliding plane of the coarse-tilting stage to detect the induced acoustic vibrations, as shown in Fig. 4.3.

A NI USB-5132 data acquisition system (National Instruments, Inc.) was connected to a computer and the accelerometer (acoustic sensor) to detect and measure the imposed frequencies and amplitudes. The vibrational acoustic signals were collected from NI Scope, a software from LabVIEW, which can fetch and analyze data of frequency, voltage amplitude, and sound intensity level. The output of the MISTRAS 1000A accelerometer was converted to acceleration data by using a conversion factor of 10 mV/g.

4.4 Image capture system for static and dynamic droplet motion

The static and dynamic motion of each droplet, including the sliding angle of the droplet with and without imposing acoustics, was recorded using a Photron SA3 High Speed camera as shown in Fig. 4.6. The high-speed camera was placed on a translation stage to be able to adjust the height of the camera and to have a good view of each droplet. During the vibration experiments, the droplet motion was recorded at a rate of 1000 frames per second with a maximum field of view of 1024x1024 pixels.



Fig. 4.6 Photron SA3 high speed camera utilized to capture droplet images

4.5 Standard surfaces

Hydrophobic and hydrophilic surfaces, such teflon (PTFE), copper and aluminum, were used to validate the droplet sliding angle models (Equations 33 and 40). Table 4.1 shows a description of the wetting characteristics of the standard surfaces that were used to validate the physics-based mathematical models. The standard surfaces consisted of teflon, copper, and aluminum. A SiO_2 surface (silicon wafer) was also used

in the study of droplet shedding for validation purposes, see Appendix A. The metal surfaces were carefully polished several times to have a very smooth and homogeneous shiny surface. Also, a functionalized copper surface was also used (i.e. hydro-copper), which contains a nanostructured oxide layer for achieving high contact angles as shown in Table 4.1. Since the surfaces are considered to be smooth surfaces with high thermal conductivity (except teflon), different droplet sizes and acoustic conditions were used when conducting droplet shedding experiments. Moreover, the same surfaces were used when conducting condensation heat transfer experiments.

Standard surface characteristics		
Surface	Contact Angle	Type of surface
Teflon	101°	Hydrophobic
Copper	81°	Hydrophilic
Hydro-Copper	153°	Super-hydrophobic
Aluminum	71°	Hydrophilic
SiO ₂	77°	Hydrophilic

Table 4.1 Description of surface wetting properties for standard surfaces

4.6 Calibration of vibrational system

All vibrational experiments data were detected using an acoustic sensor and analyzed using LabVIEW. To verify that the frequency of the vibrated system correlates well with the frequency provided by the Tone Generator software (input), a mono-frequency calibration test was performed. Fig. 4.7 demonstrates a good linearly

correlation between the input (i.e. delivered by tone generator) and output (i.e. received by acoustic sensor) imposed frequencies.

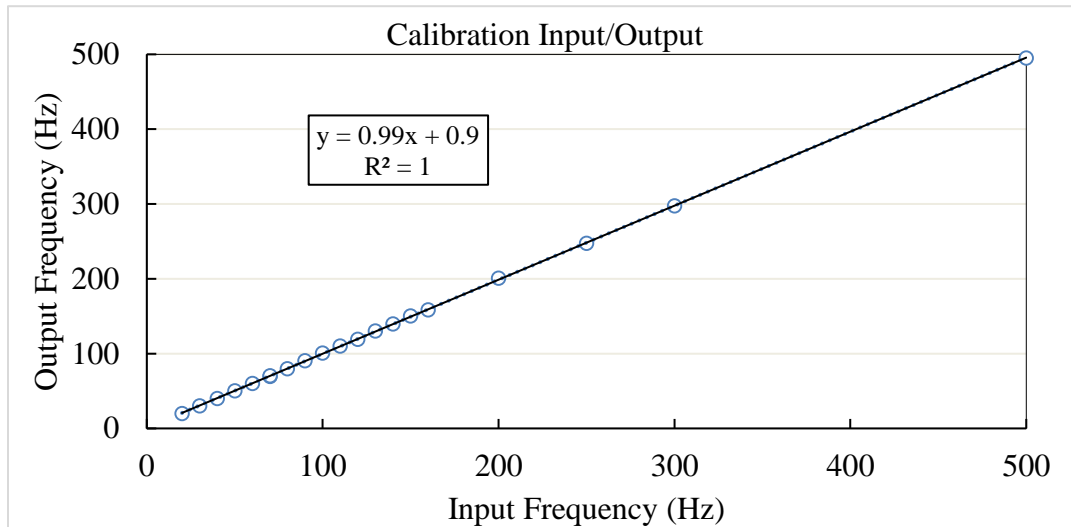


Fig. 4.7 Calibration input/output of the acoustic system

To be able to estimate sliding angle using Equation 40, the acoustic amplitude or acceleration along the sliding plane should be known. However, such information cannot be known a priori, unless the amount of vibration energy along the sliding plane is related to the imposed acoustic energy delivered by the acoustic system. To understand the relationship between the amount of vibration energy along the sliding plane and the corresponding vibration energy provided by the system, the product of the amplitude and frequency (vibration energy) along the sliding plane was correlated with the product of the amplitude and frequency delivered by the acoustic system (horizontal tilting stage, see Fig. 4.1). Therefore, a calibration test was performed to determine the relationship between the vibration energy along the sliding plane and the imposed acoustic energy.

The frequencies imposed varied from 20 Hz to 55 Hz. The calibration experiments have shown that regardless of the imposed frequencies to the system, the relationship between the imposed acoustic energy and the acoustic energy along the sliding plane correlates well as shown in Fig. 4.8. The correlation curve shown in Fig. 4.8 demonstrates that the imposed frequencies and amplitudes can be related linearly to the acoustic energy measured along the sliding plane.

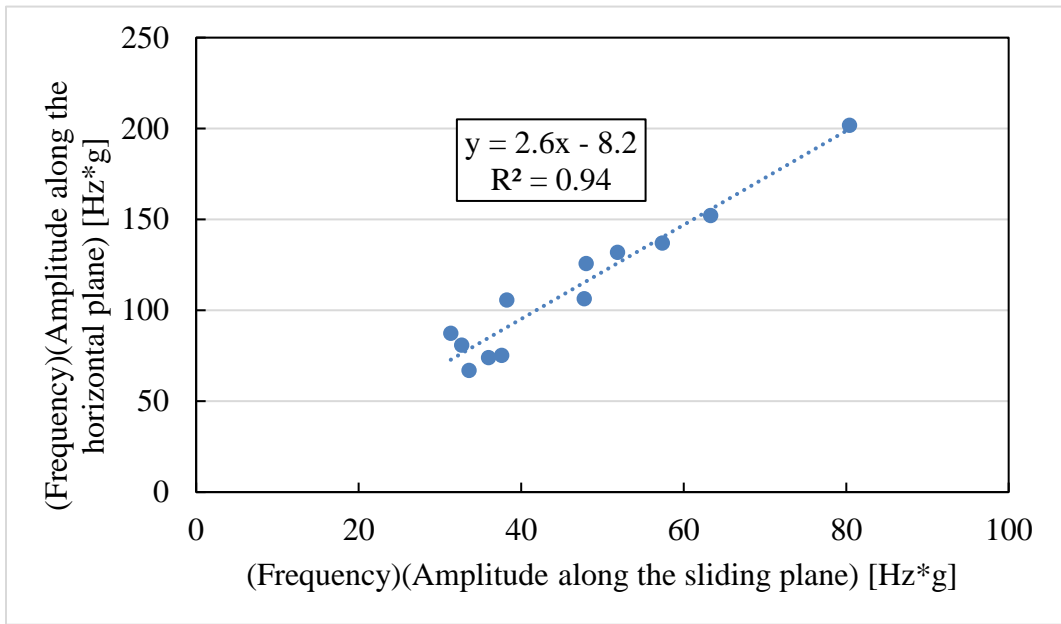


Fig. 4.8 Correlation between vibrational energies imposed on horizontal and along the sliding plane

4.7 Procedures for sliding angle experiments with and without imposing acoustics to the system

The following subsections describes how experiments were conducted to measure contact angles, receding, and advancing angles, sliding angles, droplet shape factors, natural resonance frequencies and amplitudes.

4.7.1 Contact angle measurement

To determine droplet contact angle on different surfaces, individual droplets were placed on a horizontal aligned surface by using a 10-100 μ L pipette with increments of 0.2 μ l (Gilson, Inc. Pipetman P100). The contact angle of each droplet, under static conditions, was measured from images taken by the high-speed camera using ImageJ plug-in called “Drop Shape Analysis.” Fig. 4.9 shows an image used for static droplet contact angle measurement.

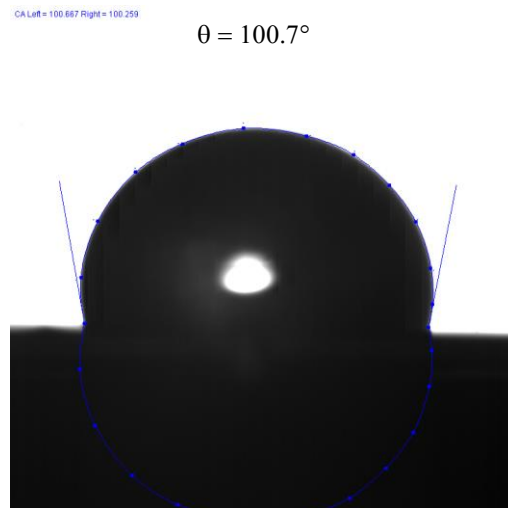


Fig. 4.9 Image used for static contact angle measurement of a 10 μ L droplet on teflon

The equilibrium contact angle can also be determined from the Young's equation [13-15], and it is found by taking the average of the advancing and receding angle of the droplet on a tilted plane (see Fig. 3.1):

$$\theta = \frac{\theta_{adv} + \theta_{rec}}{2} \quad (41)$$

Equation 41, which considers equilibrium contact angle, contact angle hysteresis, and droplet volume, has been validated experimentally, as shown in the results chapter.

4.7.2 Sliding angle measurement for non-vibrational cases

The sliding angle of the droplet is found from placing a droplet on an inclined surface at different inclination angles. The droplet starts sliding off the surface when the inclination angle is increased. If the droplet becomes steady on the inclined surface, the fine-tilting stage is slowly adjusted until the droplet becomes unsteady and begins to move slowly. An image of the sliding droplet was taken by using the high-speed camera. By using the image-processing software, the inclination angle, advancing, and receding angle were measured based on the image taken as shown in Fig. 4.10.

CA Left = 112.060 Right = 87.287

$$\theta_{\text{rec}} = 87.3^\circ$$

$$\theta_{\text{adv}} = 112.1^\circ$$

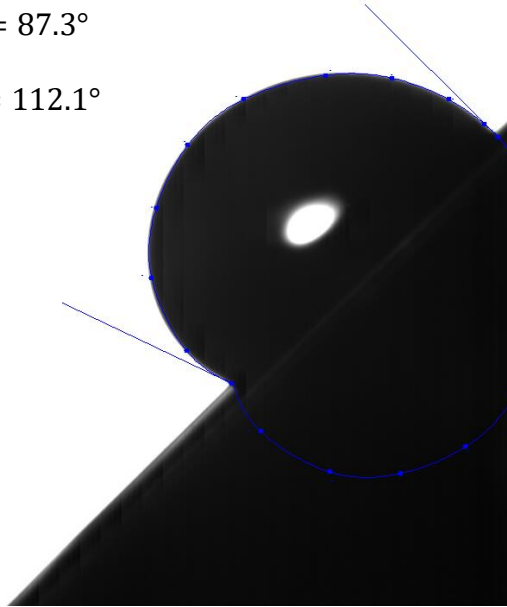


Fig. 4.10 Measurement of advancing and receding angle when the droplet starts sliding off the surface using a 10 μ L teflon

4.7.3 Droplet aspect ratio

Based on previous studies, knowing the projected droplet aspect ratio is important for being able to estimate the retentive force of sliding droplets. Extrand [27] developed a correlation which relates the droplet's aspect ratio to the retentive force based on contact angle hysteresis. In Fig. 4.11, it illustrates the elongation of the droplet on an inclined surface. The aspect ratio of the droplet, β , is based on measuring the length and width of the droplet. Then, the retentive force constant (or numerical constant in [27]), k , is calculated from Equation 10. The correlation is used to calculate k , which is then used to precisely estimate droplet sliding angle using Equations 33 and 40.

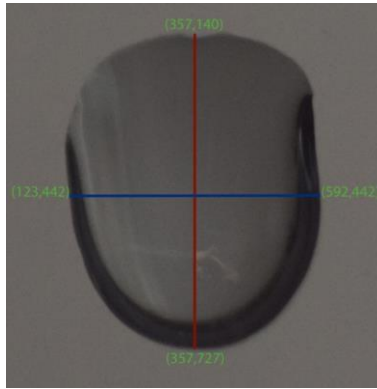


Fig. 4.11 Water droplet on inclined surface used to determine aspect ratio, β

4.7.4 Resonance frequency of droplets

Studies have shown that to reduce the sliding angle of the droplet efficiently, a resonant frequency for each droplet should be imposed [35]. In this study, vibrations were imposed by using a speaker, as shown in Fig. 4.1. The acoustic data were detected from an acoustic sensor and were analyzed using a data acquisition system. The vibrational values were theoretical calculated from the Noblin's model (Equation 13), which is based on droplet volume, droplet contact line and contact angle, and resonance node number (discussed in Section 2.2.2). The fundamental idea of the model is to identify the mobility and the suitable frequency of each droplet-surface combination that may reduce droplet-sliding angles. To that end, the imposed frequency, depending on the droplet volume, was determined to see if the resonant frequency induced higher lateral motion for each droplet sitting on a surface. The first and second resonance modes of vibrations were considered to determine which one (first or second) was more effective in terms of sliding angles for all droplet-surface combinations.

4.7.5 Sliding angle of droplets when imposing acoustics to the system

Droplets were first placed on a horizontal-inclined surface and vibrations were imposed to observe the resonant frequency that showed the higher lateral motion within the first two resonance modes of vibrations. Then, the tilting-stage was inclined until the droplet became steady. Induced-vibrations to the system were imposed and the tilting-stage was further adjusted until the droplet became unsteady and slid off the surface. Images were taken by the high-speed camera at 1000 fps and overlaid to identify the vibrational nodes and pattern for each droplet-surface condition. Also, inclination angle was captured for each droplet sliding to measure the sliding angle. Fig. 2.6 shows the droplet resonance motion with wave nodes that corresponds to the first and second resonance mode of vibrations, respectively. Results have indicated that imposing vibrations to the system, the resonant frequency lead to a reduction in sliding angles.

4.7.6 Measuring acceleration for validating developed physics-based mathematical models

When imposing vibrations to the system at a specific inclination angle, droplet sliding angle reduces compared to the non-vibrational sliding angle conditions. An accelerometer was attached along the sliding plane to obtain experimental acceleration values in m/s^2 as detected by the NI-Scope software. For each predicted theoretical resonant frequency (Equation 13), a specific amplitude or acceleration was obtained experimentally. Therefore, the amplitude obtained was recorded and used in Equation 40 to validate the model and to compare the theoretical with experimental results. The

results show that Equation 40 is in a good accordance with experimental data and can be used effectively to relate imposed resonance frequencies to critical sliding angle of droplets.

4.8 Dropwise condensation

After conducting droplet sliding angle experiments, it became clear that imposed acoustic vibrations should indeed facilitate droplet shedding during condensation. A recent study shows that it is possible to enhance the condensation heat transfer rate by using a mechanical vibrational system [9]. To understand better the role of induced acoustics on dropwise condensation, an experimental setup has been designed and tested. The condensation experimental setup consists of five main operating components: Peltier cell, humidifier, power supply, data acquisition system and temperature controller, as shown in Fig. 4.12 and Fig. 4.13. The following subsections describe the experimental procedures used to determine the condensation heat transfer rate from standard surfaces (Table 4.1), including a hydrophobic (painted metallic) aluminum surface, with and without the imposed of acoustics into the system.

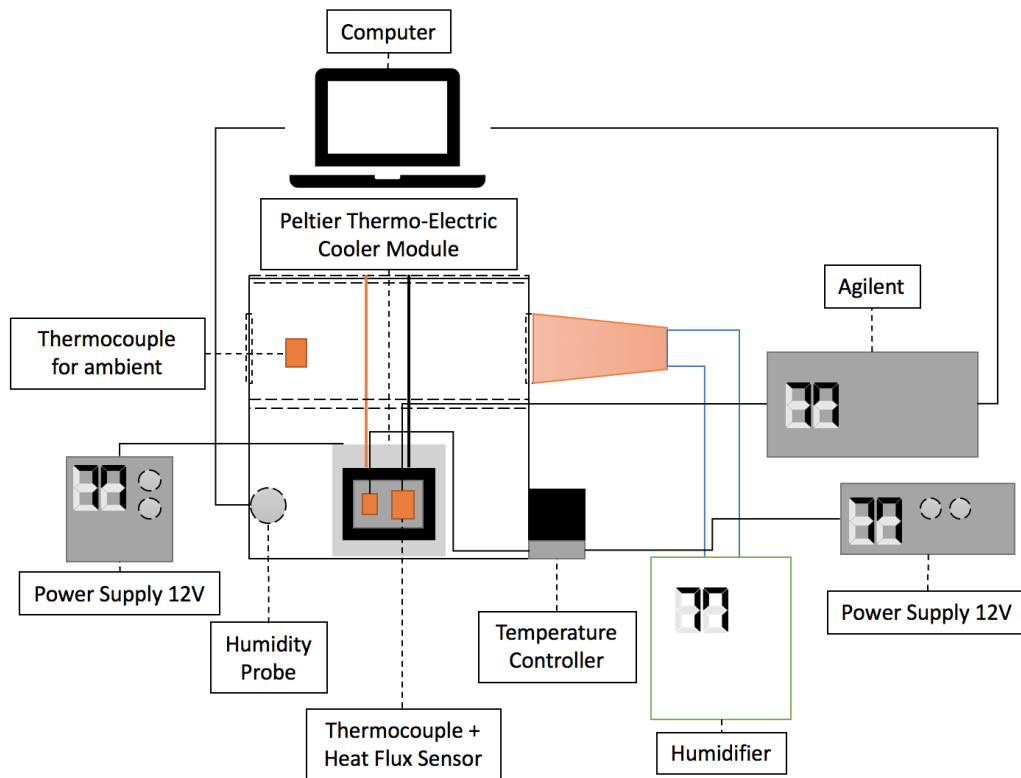


Fig. 4.12 Acoustic-induced condensation system I

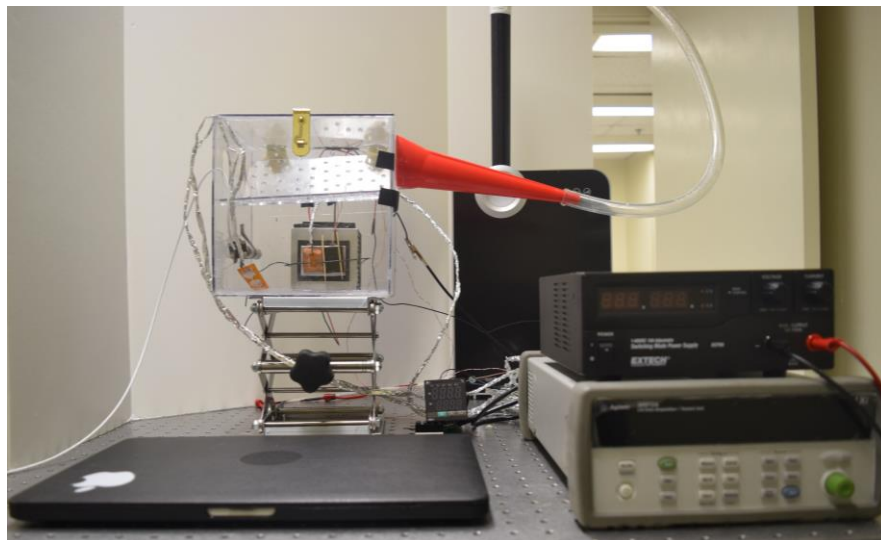


Fig. 4.13 Acoustic-induced condensation system II

4.8.1 Description of the condensation components

The internal components, e.g. Peltier module, humidity probe, heat flux sensors, thermocouples, were mounted inside a 20 cm x 20 cm designed clear polycarbonate sheet box condensation system (Fig. 4.12). In this study, the main components of the condensation experiment, the Peltier thermo-electric cooler module, the temperature controller, the humidifier and the HFS-4 heat flux sensor, are described below.

The Peltier Thermo-electric cooler module, as shown in Fig. 4.14, was used to conduct the condensation experiments since condensation occurs when the surface temperature of the substrate is lower than the dew point temperature.

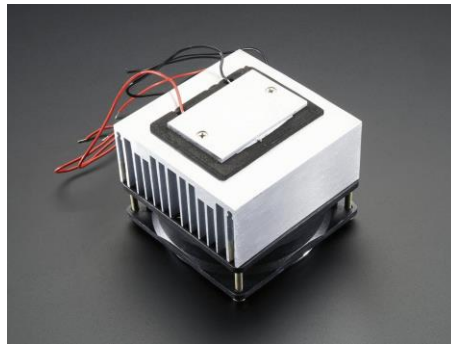


Fig. 4.14 Peltier Thermo-Electric Cooler Module and Heatsink Assembly [42]

When the Peltier module is connected to a power supply, the module cools down at a minimum temperature of $-16\text{ }^{\circ}\text{C}$, which creates crystalized droplets and may affect the condensation study. To avoid temperatures below 0° , a temperature controller connected to a power supply, as shown in Fig. 4.15, has been installed to the module to control and monitor surface temperatures. To control the temperature of the module, a

type-T thermocouple was placed on the surface's module and connected to the temperature controller. In this study, surface temperatures of the module and standard surfaces (Table 4.1) were varied from 2°C to 15°C to understand the role of surface temperature on heat flux with and without imposing acoustics on the surface.



Fig. 4.15 Fuji Electric PXR4 Temperature Controller [43]

A humidifier, as shown in Fig. 4.16, has been installed to create a moist air environment in the system to enable dropwise condensation. One inlet and two outlets were perforated in the polycarbonate box so moist air could enter and exit the open condensation system. Since the system was open, all condensation experiments were conducted in the presence of non-condensable gases (i.e. air). To prevent a large moisture environment inside the condensation system, a perforated polycarbonate sheet was designed and placed above the Peltier module to regulate the amount of mist or moist air interacting with the surface. The humidity ratio was measured by using a humidity and temperature sensor with USB output (Omega). Humidity ratio data was obtained from the TRH Central (Omega Engineering, Inc.) software.



Fig. 4.16 PureGuardian H8000B Ultrasonic Warm and Cool Humidifier [44]

Thin film heat flux sensor models HFS-3 and HFS-4 (Omega Engineering, Inc.), with a type-K thermocouple integrated, were used to measure the heat flux and surface temperature in each surface case. The heat flux sensor (HFS-4) was sandwiched between similar standard surfaces and placed on the surface of the module, as shown in Fig. 4.17. The heat flux sensors were connected to an Agilent data acquisition system to measure heat flux and surface temperatures.

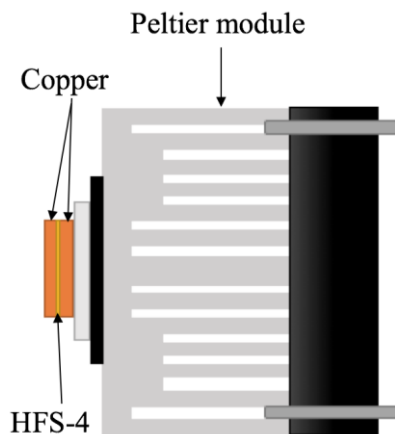


Fig. 4.17 HFS-4 sandwiched between similar standard surfaces

4.8.2 Calibration of thermocouples and heat flux sensor

The thermocouples and heat flux sensors were calibrated to ensure reliable surface temperature and heat flux measurements. The type-K thermocouples were attached on top of the Peltier module's surface and connected to a DAQ. Both thermocouples depict similar temperature readings when different surface temperatures were imposed by the Peltier module.

To calibrate the heat flux sensor (HFS-4), a calibration system was developed to measure the surface temperature and heat flux within a medium consisting of a metallic-aluminum cone to ensure uniform heat flux. Aluminum and copper surfaces were used for heat flux and surface temperature measurements because of their good thermal conductivity values. The thermal conductivity of copper and aluminum is about $3.88 \frac{\text{W}}{\text{cm K}}$ and $1.67 \frac{\text{W}}{\text{cm K}}$, respectively. The sample's thickness was approximately 0.3175 cm. The entire system was insulated to minimize any heat losses. The insulated metallic aluminum cone was placed below a heater plate for ensuring uniform heat conduction, as shown in Fig. 4.18.

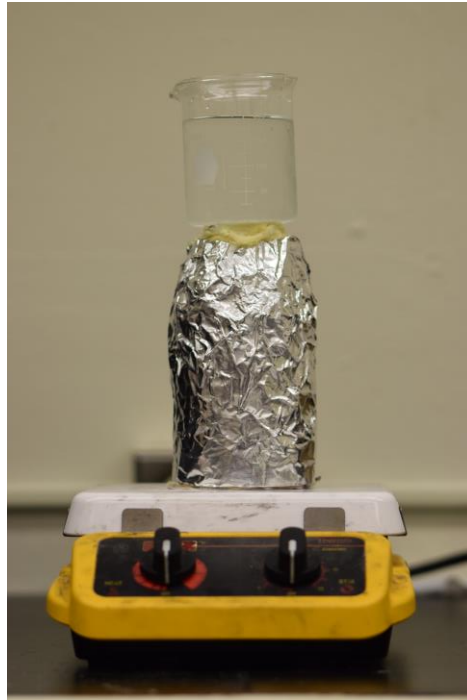


Fig. 4.18 Calibration system using a heater plate

Copper (orange) and aluminum (grey) surfaces, as shown in Fig. 4.19, were positioned and sandwiched within the heat flux and temperature (thermocouple) sensors (HFS-3 and HFS-4) and placed on top of the hot medium. The heat flux sensor (HFS-4) used during the experiments has an accuracy of $\pm 2\%$. A beaker with cold water and ice was placed on top of the standard surface for greater surface temperature gradient and heat flux. An average period of 60 sec was used for recording heat flux and surface temperature values. Results were acquired using the Agilent data acquisition system and were analytical analyzed using Excel. Results show a good correlation between heat flux (W/cm^2) and voltage (mV) ratio when different numbers of surfaces were used, as shown in Fig. 4.19.

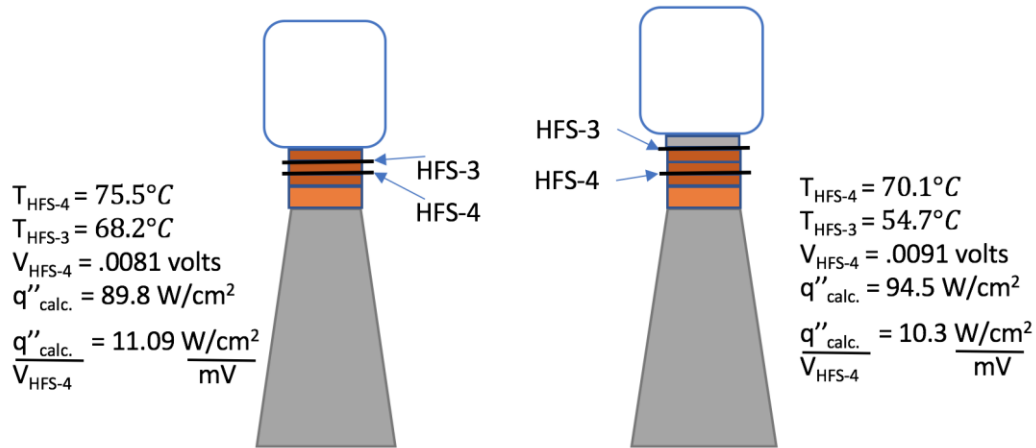


Fig. 4.19 Schematic of the heat flux and thermocouple calibration system

4.8.3 Dropwise condensation experiment protocols

Four different types of good conductive materials including super-hydrophobic copper, copper, aluminum and hydrophobic metallic surface (painted aluminum) were used in the condensation experiments with and without imposing acoustic stimuli. The dimensions of the materials were cut to be 2.5cm by 2.8cm to match the same dimensions as the heat flux sensors. A thermocouple type-T was placed on the cold-side of the Peltier module, which was aligned vertically to allow for adequate droplet shedding. The thermocouple was connected to a temperature controller to control the surface temperature of the Peltier, as described above. The Peltier module surface temperature was varied from 2°C to 15°C . All experiments were conducted in a 5-minute period for each fixed surface temperature condition. The ambient temperature was in the range of 21 to 22°C .

The humidifier was used to create moist air inside the open condensation system as described above. The TRH Central software was used to fetch the humidity ratio data

detected by the humidity probe. The acquired humidity ratio data were then recorded and analyzed using Excel.

Two of the same standard surfaces (aluminum and copper) were placed on the surface of the module. The HFS-4 sensor, with same surface dimension, was sandwiched between both surfaces (see Fig. 4.17). An Agilent bench-link data logger software was used to fetch heat flux and surface temperature data detected by the HFS-4. The HFS-3 thermocouple was used to measure the ambient temperature inside the condensation system. The acquired data were recorded and analyzed using Excel.

Experiments were conducted when acoustics were absent and present in the condensation process. The condensation system was placed on top of a speaker (Fig. 4.12) and the imposed sweep frequency response was varied from 20 Hz to 60 Hz depending on the resonant frequency for each droplet-surface combination based on the corresponding wetting characteristics. Images and videos of droplet-surface combinations were recorded during the condensation process when acoustic stimuli were imposed. In addition, droplet size distribution of each surface was obtained from images taken during condensation. Based on experimental results, empirical correlations for dropwise condensation under the effects of acoustic streaming on hydrophilic and hydrophobic surfaces were postulated and validated, as shown in the next chapter.

5. RESULTS AND DISCUSSION

In this chapter, droplet characteristics and sliding on standard surfaces are presented based on experimental data and theoretical calculations. In addition, resonant frequencies and amplitudes were identified through calculations and verified via measurements to validate the acoustic model. The relationships between the first two resonance modes of vibrations were studied as a baseline to understand droplet motion behavior and to overcome the energy barrier caused by the droplet hysteresis effect to facilitate sliding. As a result, once the theoretical model has been proven with and without imposing vibrations, the effects of acoustics on condensation was also studied to determine if induced-acoustics enhance the overall heat transfer performance through enhanced droplet shedding events.

5.1 Validating the droplet sliding angle model without the effects of acoustics

The theoretical sliding angle values for individual droplets were calculated from Equation 33. From the model, the gravitational acceleration g was set to 9.81 m/s^2 , the surface tension γ_{LG} was set to 0.072 N/m (surface tension of water in air at $25 \text{ }^\circ\text{C}$), density of the water ρ was set to 998.2 kg/m^3 (density of water at $25 \text{ }^\circ\text{C}$), and the other terms including static contact angle, droplet radius, advancing angle and receding angle, and k were calculated from experimentation. The droplet radius was obtained from Equation 16 based on droplet contact angle and droplet volume. The advancing and receding angle ($\Delta\theta$) and contact angle (θ) of the droplet were obtained from images taken by the high-speed camera at the moment when each droplet slowly slides off the

surface. The retentive force constant, see Section 4.7.3, was obtained from an image of the projected view of the sliding droplet, as shown in Fig. 4.11. Each image was then processed by an image-processing software to measure receding and advancing angle, and critical inclination angle, as shown in Fig. 5.1.

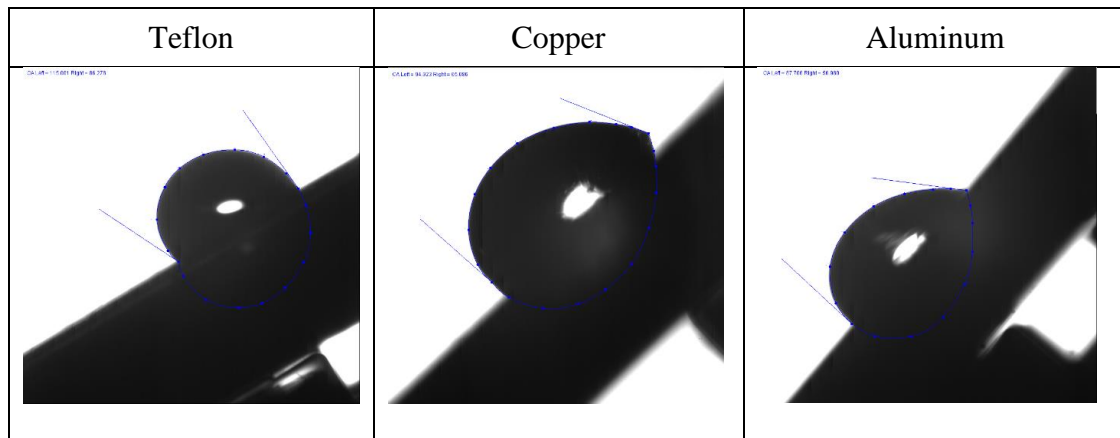


Fig. 5.1 Measurement of advancing and receding angle when droplet start sliding off the surface without imposing acoustics

Based on experimental observations during droplet sliding, hydrophobic surfaces depict better sliding than those surfaces with hydrophilic characteristics. Fig. 5.2 shows that sliding angle decreases with increasing droplet volume for all cases.

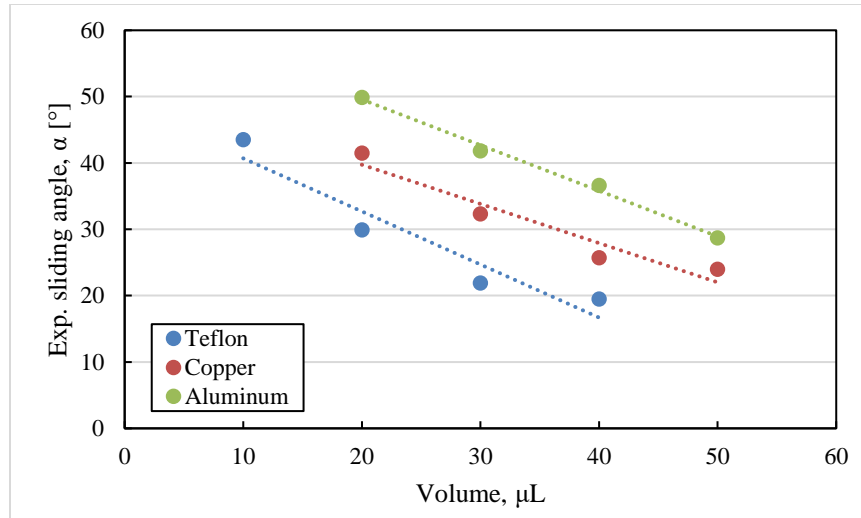


Fig. 5.2 Relationship between droplet volume and sliding angle

A recent study by Pierce *et al.* [45] observed a similar trend in which bigger droplets exhibit better shedding with higher contact angles. In a recent study by Bommer *et al.* [15] showed that contact angle hysteresis increased with droplet volume slightly; however, contact angle hysteresis increases significantly with tilting or sliding angle. Fig. 5.3(a) shows contact angle hysteresis is directly proportional to droplet volume. Furthermore, Fig. 5.3(b) shows that sliding angle is inversely proportional to contact angle hysteresis. Moreover, the experimental data show that hydrophilic surfaces depict higher contact angle hysteresis than a hydrophobic surface for the same sliding angles. In general, larger droplets overcome the energy barrier more than smaller droplets regardless of surface type, because the associated retentive force is inversely proportional to contact angle when considering the same droplet volume.

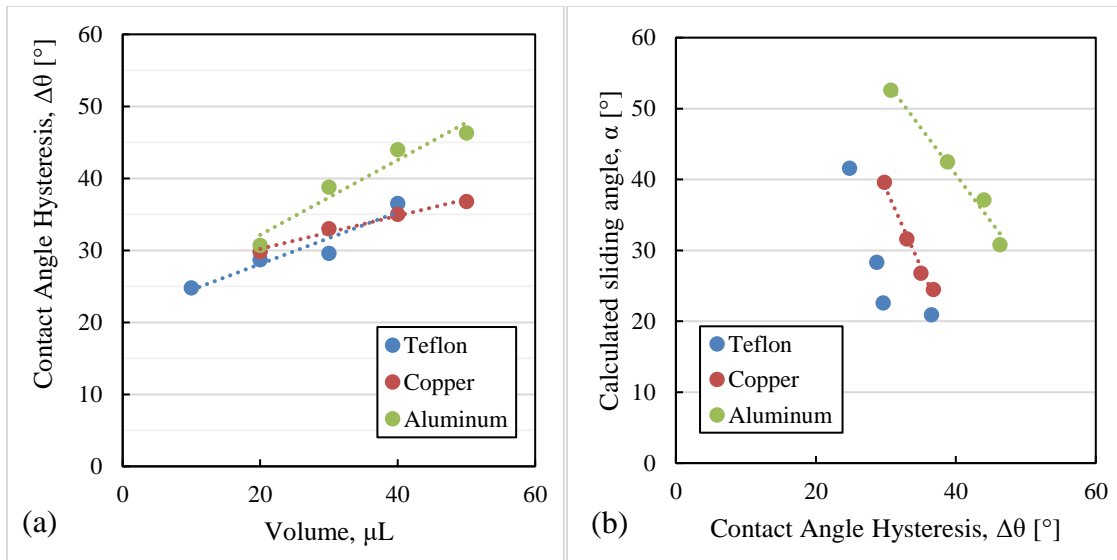


Fig. 5.3 (a) Relationship between contact angle hysteresis and droplet volume, and (b) relationship between sliding angle and contact angle hysteresis

As part of the study, the calculated sliding angles acquired from the model were compared with experimental results, as shown in Tables 5.1 through 5.3. Copper depicts better correlation based on theoretical and experimental data with a 3.5% relative error. Based on all experimental results, the theoretical sliding model is in a good accordance with experimental sliding data with a combined relative error of 4.5%, as shown in Fig. 5.4. Therefore, the theoretical values can be used effectively to relate contact angle hysteresis and static contact angle to critical sliding angle of droplets. In addition, experiments show that the contact angle of the droplet remains constant regardless of droplet size or volume, as expected.

Surface	Volume [μL]	θ_{adv}	θ_{rec}	$\Delta\theta$	k	α_{theo}	α_{exp}	Error
Teflon $\theta=101.3^\circ$	10	112.1°	87.3°	24.8°	1.4	41.6°	43.5°	-4.2%
	20	115.0°	86.3°	28.7°	1.4	28.3°	29.9°	-5.2%
	30	115.4°	85.8°	29.6°	1.4	22.6°	21.9°	3.5%
	40	122.4°	85.9°	36.5°	1.4	20.9°	19.5°	7.3%

Table 5.1 Droplet theoretical and experimental data without imposed vibrations on teflon surface

Surface	Volume [μL]	θ_{adv}	θ_{rec}	$\Delta\theta$	k	α_{theo}	α_{exp}	Error
Copper $\theta=80.8^\circ$	20	94.9°	65.1°	29.8°	1.5	39.6°	41.5°	-4.6%
	30	97.5°	64.5°	33.0°	1.5	31.6°	32.3°	-2.1%
	40	98.3°	63.3°	35.0°	1.4	26.8°	25.7°	4.4%
	50	99.8°	63.0°	36.8°	1.5	24.5°	24.0°	2.2%

Table 5.2 Droplet theoretical and experimental data without imposed vibrations on copper surface

Surface	Volume [μL]	θ_{adv}	θ_{rec}	$\Delta\theta$	k	α_{theo}	α_{exp}	Error
Aluminum $\theta=71.1^\circ$	20	87.7°	57.0°	30.7°	1.7	52.6°	49.9°	5.4%
	30	90.7°	51.9°	38.8°	1.5	42.5°	41.8°	1.6%
	40	92.3°	48.3°	44.0°	1.5	37.1°	36.6°	1.4%
	50	93.7°	47.4°	46.3°	1.4	30.8°	28.7°	7.3%

Table 5.3 Droplet theoretical and experimental data without imposed vibrations on aluminum surface

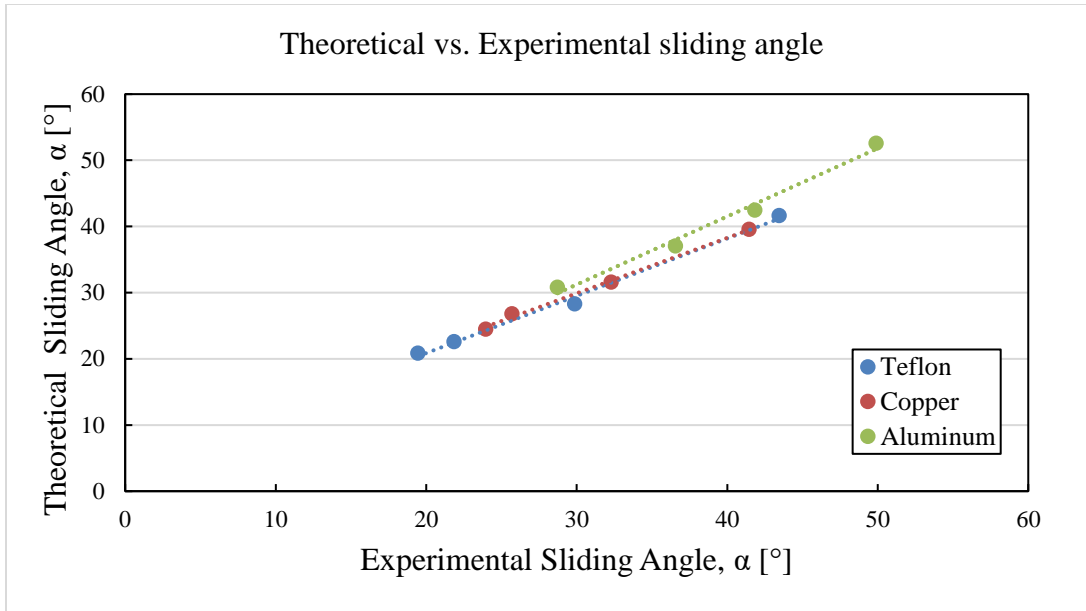


Fig. 5.4 Comparison of the theoretical and experimental values based on sliding terms

5.2 Resonance frequencies and resonance modes of vibrations using the Noblin's model

This section presents the theoretical and experimental results for droplet resonance motion obtained from Equation 13. An investigation of the droplet motion behavior depending on the resonance mode of vibration is presented. In addition, this section discusses which of the first two resonant modes of vibrations (1st and 2nd resonance mode) leads to better lateral motion to overcome the energy barrier caused by hysteresis in terms of sliding angles.

5.2.1 Calculated resonance frequency

The theoretical resonant frequencies were acquired from using the Noblin's model (Equation 13), as mentioned in Section 2.3. The gravitational acceleration, surface

tension and density of water were set, as discussed in Section 5.1. The calculated results are shown in Table 5.4.

		1 st Natural Frequency (Hz) j = 1.5			2 nd Natural Frequency (Hz) j = 2.0		
		20	30	40	20	30	40
Surface	Vol (μL)						
	Teflon	39	32	28	70	58	50
	Copper	39	33	29	74	61	53
	Aluminum	38	32	28	73	60	53

Table 5.4 Calculated resonance frequencies for different droplet volumes and different surfaces

Based on the theoretical values, distinctive droplet motion behavior should be observed during the resonant mode of vibrations is imposed. The resonance modes of vibrations (j) were set to be $j = 1.5$ for the first resonance mode and $j = 2.0$ for the second resonance mode. At the first resonance mode, the vibrated droplet should be expected to exhibit a high lateral motion as shown in Fig. 5.5(b). Recent studies have shown that the droplet lateral resonant motion is the most effective in terms of droplet motion, as advancing angle increases and receding angle decreases [33-35]. Furthermore, strong vibrational stimulus leads to greater dynamic contact angle hysteresis, which helps overcome the energy barrier associated with the retentive force [34]. At the second resonance mode of vibrations, the droplet exhibits a continuously combined vertical-horizontal motion [10], where advancing and receding angle alternates from every motion, as shown in Fig. 5.5(c). In summary, a previous study [10] has observed the same expected droplet motion when the first and second resonance modes are imposed.

Specifically, three and four number of nodes along the droplet profile can be identified when imposing first and second resonance modes, respectively, as shown in Fig. 5.5. The location of the nodes for the experimental cases are presented in the next section.

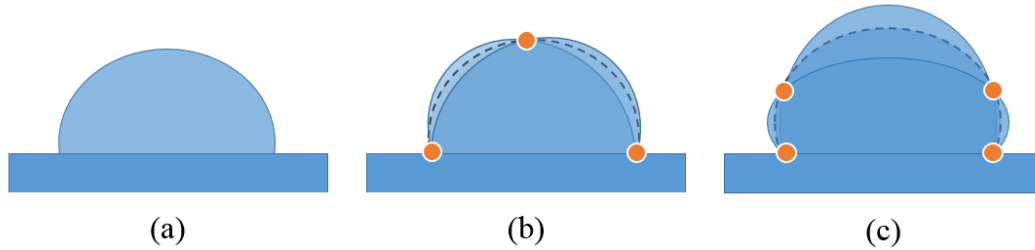


Fig. 5.5 Representation of expected droplet motion for (a) non-vibration case, (b) the first resonance mode and (c) the second resonance mode. Colored dots represent number of nodes.

5.2.2 Experimental resonance frequency using the first and second resonance modes of vibration

The experimental frequency was observed when the droplets were resting on both the horizontal and inclined planes to see the highest level of lateral and horizontal-vertical motion at each resonant frequency. Table 5.5 shows the frequency values measured that corresponds to the number of nodes observed in each droplet when the resonant frequency was induced or applied on the system, which depends on droplet volume and contact angle, as shown in Fig. 5.6.

		1 st Natural Frequency (Hz) j = 1.5			2 nd Natural Frequency (Hz) j = 2.0		
		20	30	40	20	30	40
Surface	Vol (μL)						
	Teflon	39	32	27	71	58	50
	Copper	37	31	28	70	57	51
	Aluminum	36	30	26	69	56	53

Table 5.5 Experimental resonance frequencies for different droplet volumes and different surfaces

As shown in Table 5.5, the corresponding imposed resonant frequencies are slightly lower than the calculated resonance frequency. Noblin observed a similar trend in his study based on acoustic experiments [10]. Knowing the optimal resonance frequency in horizontal cases for the corresponding modes of vibrations, the effects of vibrations under the influence of gravity on inclination angles should be explored.

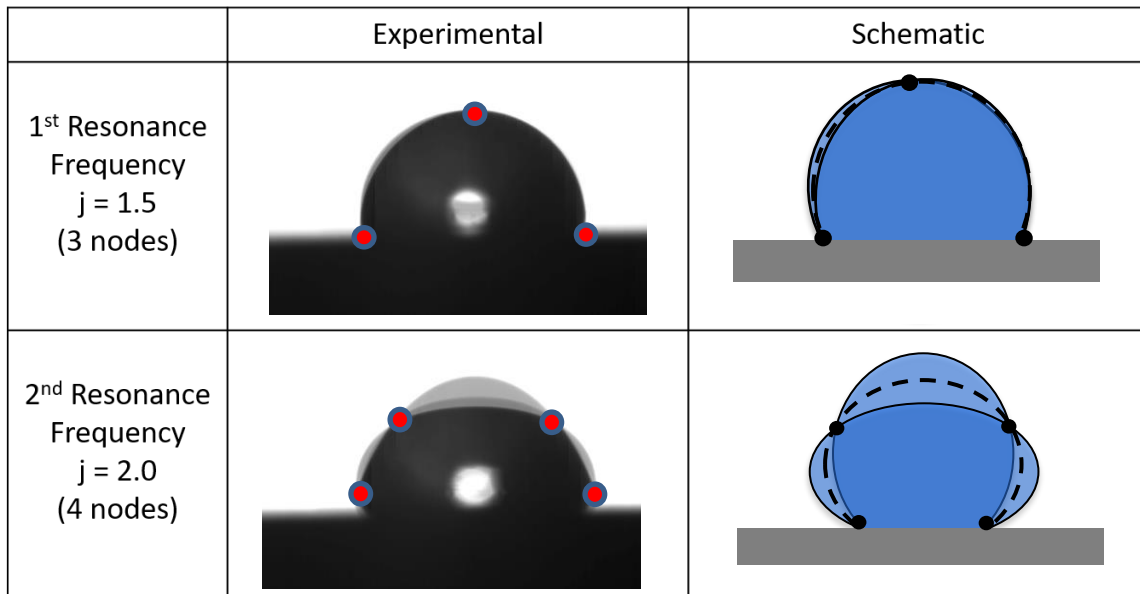


Fig. 5.6 Droplet resonance mode of vibrations using a 10μL droplet on a teflon

5.3 Validating the droplet sliding angle model under the effects of acoustics

The effects of the first and second resonance mode of vibrations were studied to understand droplet behavior on inclined surfaces. Although Equation 40 is independent of resonant frequencies, the amplitudes of vibrations were obtained from the optimal vibration (i.e. resonant condition) of the droplet. Equation 40 used the same experimental results as shown in Section 5.1, including the same surface tension, density, static contact angle, advancing angle and receding angle, k value, and the acceleration magnitude measured, as shown in Fig. 4.8.

In order to understand the effects of resonant frequencies on the reduction of sliding angle when using different standard surfaces, a set of experiments were performed based on the experimental resonant frequencies shown in Section 5.2.2 for an inclined plane. In general, at the inclined plane, the droplet motion for the first resonance mode of vibrations depicted stronger lateral motion than those at the second resonance mode, as shown in Fig. 5.7. When imposing the first resonance mode, droplet motion exhibits a higher lateral motion, which leads to higher advancing angle. Therefore, it is assumed that the vibration oscillation force is large enough to counteract the retentive force effects (i.e. caused by surface tension). As a result, the droplets can slide downwardly at a lower inclination angle [33, 35, 46].

From Fig. 5.8, the first resonance frequency (or mode) leads to lower sliding angles than the second resonant frequency [46]. In summary, lower resonant frequencies are better for droplet sliding than higher resonant frequencies (or modes) [46].

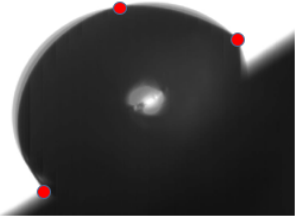
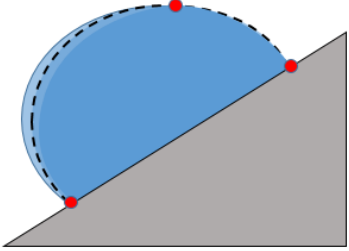
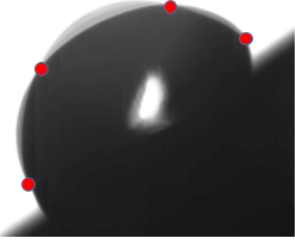
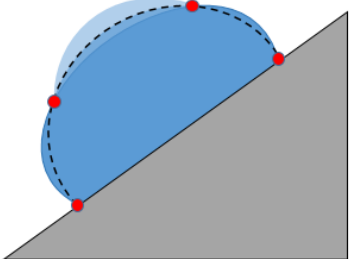
	Experimental	Schematic
1 st Resonance Frequency $j = 1.5$ (3 nodes)		
2 nd Resonance Frequency $j = 2.0$ (4 nodes)		

Fig. 5.7 Vibrations at two distinct resonance modes of a 20 μ L droplet on copper surface on an inclined plane

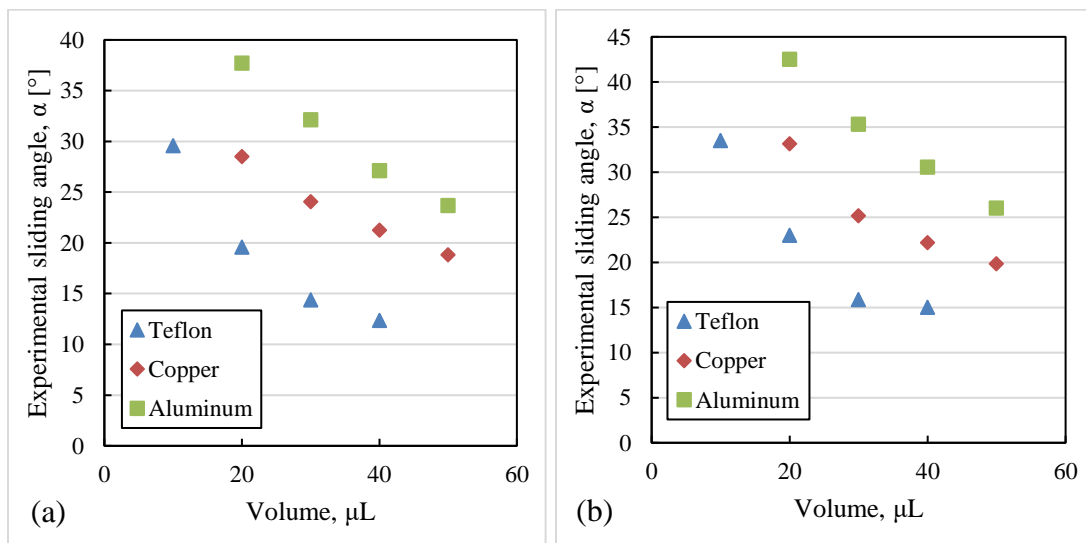


Fig. 5.8 Relationship between droplet volume and sliding angle for (a) the first resonance mode and (b) the second resonance mode

As discussed above, the associated retentive force is inversely proportional to contact angle for the same droplet volume. Furthermore, droplets with lower surface contact area (i.e. higher contact angle at the same volume) are less likely to remain on the surface. Based on vibrational experimental results, hydrophobic surfaces (i.e. teflon) are better in terms of sliding when imposing the 1st resonant mode of vibration than hydrophilic surfaces (i.e. copper and aluminum), as shown in Fig. 5.9. The enhancement in terms of experimental sliding for teflon, while imposing the 1st resonant mode was approximately 34%, whereas copper and aluminum surfaces had enhancements of 31% and 24%, respectively. The second resonant mode of vibration exhibits a continuously combined vertical-horizontal motion in the droplet, which leads to lower dynamic contact angle hysteresis. As a result, the second resonant mode does not lead to a significant enhancement in terms of sliding angle.

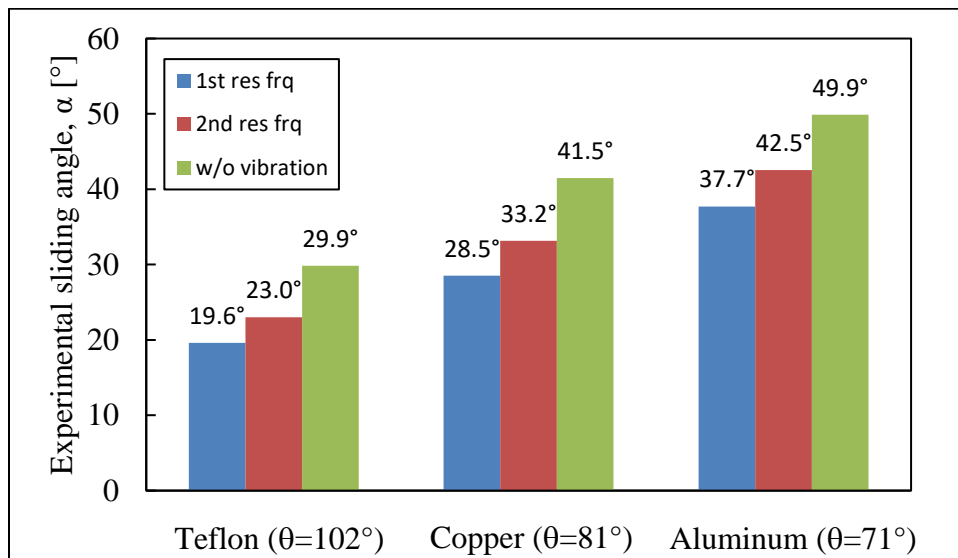


Fig. 5.9 The sliding angle of 20 μL droplet at different resonant frequencies

To understand the effects of acoustic on droplet sliding, the imposed acceleration and frequency values were correlated to the measured (or received) acceleration and frequency values along the sliding plane, as shown in Fig. 4.8. By using the correlation in Fig. 4.8, the corresponding sliding angles were estimated using Equation 40 as shown in Tables 5.6 to 5.11. As the tables show, the resonant frequencies necessary for adequate droplet sliding are inversely proportional to droplet volume. For all hydrophilic surfaces (i.e. copper and aluminum) under the effects of the first resonance mode, the acoustic acceleration along the sliding plane is inversely proportional to droplet volume, which clearly suggests that bigger droplets need to be excited less to promote adequate droplet shedding. However, in the case of teflon, the acoustic acceleration is relatively constant with respect to droplet volume.

Tables 5.6 to 5.11 also show that the sliding angles calculated using Equation 40 match well with the experimental sliding angles. Based on error propagation statistical analysis, the error associated with the model is $\pm 10.6\%$ of the experimental values, as shown in Fig. 5.10. Fig. 5.11 shows a good linear correlation between the model and experimental values for the first and resonance mode of vibrations with a R^2 value of 0.98. Therefore, the results indicate that the acoustic-based droplet sliding model can be used effectively to relate imposed resonance frequencies to critical sliding angle of droplets.

Surface	Volume [μL]	$\omega_{j,res. freq.}$ [Hz]	$\omega_{j,imp. freq.}$ [Hz]	a_0 [g]	α_{theo}	α_{exp}	Error
Teflon	10	53.2	47.4	1.5	30.7°	29.6°	3.9%
	20	38.6	38.8	1.3	19.8°	19.6°	0.9%
	30	32.2	31.9	1.5	13.4°	14.4°	-6.9%
	40	28.1	27.1	1.3	12.7°	12.4°	3.0%

Table 5.6 Acoustic model and experimental data for the first resonance mode on teflon surface

Surface	Volume [μL]	$\omega_{j,res. freq.}$ [Hz]	$\omega_{j,imp. freq.}$ [Hz]	a_0 [g]	α_{theo}	α_{exp}	Error
Copper	20	38.9	36.8	1.7	27.9°	28.5°	-2.3%
	30	32.5	31.3	1.3	22.9°	24.1°	-4.9%
	40	28.6	28.0	1.2	19.4°	21.3°	-8.7%
	50	25.9	23.1	1.0	18.2°	18.8°	-3.1%

Table 5.7 Acoustic model and experimental data for the first resonance mode on copper surface

Surface	Volume [μL]	$\omega_{j,res. freq.}$ [Hz]	$\omega_{j,imp. freq.}$ [Hz]	a_0 [g]	α_{theo}	α_{exp}	Error
Aluminum	20	38.1	36.0	2.0	36.3°	37.7°	-3.9%
	30	31.6	32.4	1.5	31.5°	32.2°	-2.1%
	40	27.7	27.6	1.3	27.8°	27.1°	2.5%
	50	25.2	25.1	1.3	22.1°	23.7°	-6.8%

Table 5.8 Acoustic model and experimental data for the first resonance mode on aluminum surface

Surface	Volume [μL]	$\omega_{j,res. freq.}$ [Hz]	$\omega_{j,imp. freq.}$ [Hz]	a_0 [g]	α_{theo}	α_{exp}	Error
Teflon	10	98.7	99.0	1.3	32.0°	33.5°	-4.5%
	20	70.4	70.9	1.2	20.8°	23.0°	-9.4%
	30	58.1	57.7	1.0	15.6°	15.9°	-1.8%
	40	49.9	49.9	1.0	14.8°	15.0°	-1.6%

Table 5.9 Acoustic model and experimental data for the second resonance mode on teflon surface

Surface	Volume [μL]	$\omega_{j,res. freq.}$ [Hz]	$\omega_{j,imp. freq.}$ [Hz]	a_0 [g]	α_{theo}	α_{exp}	Error
Copper	20	73.9	69.9	1.2	31.2°	33.2°	-6.0%
	30	60.9	57.5	1.2	23.9°	25.2°	-5.0%
	40	53.2	50.5	1.0	20.5°	22.2°	-7.9%
	50	47.9	47.7	0.8	19.2°	19.9°	-3.1%

Table 5.10 Acoustic model and experimental data for the second resonance mode on copper surface

Surface	Volume [μL]	$\omega_{j,res. freq.}$ [Hz]	$\omega_{j,imp. freq.}$ [Hz]	a_0 [g]	α_{theo}	α_{exp}	Error
Aluminum	20	73.4	69.4	1.3	41.1°	42.5°	-3.2%
	30	60.4	56.2	1.3	32.6°	35.3°	-7.6%
	40	52.6	53.2	1.0	30.0°	30.6°	-1.7%
	50	47.4	47.7	0.9	24.8°	26.0°	-4.7%

Table 5.11 Acoustic model and experimental data for the second resonance mode on aluminum surface

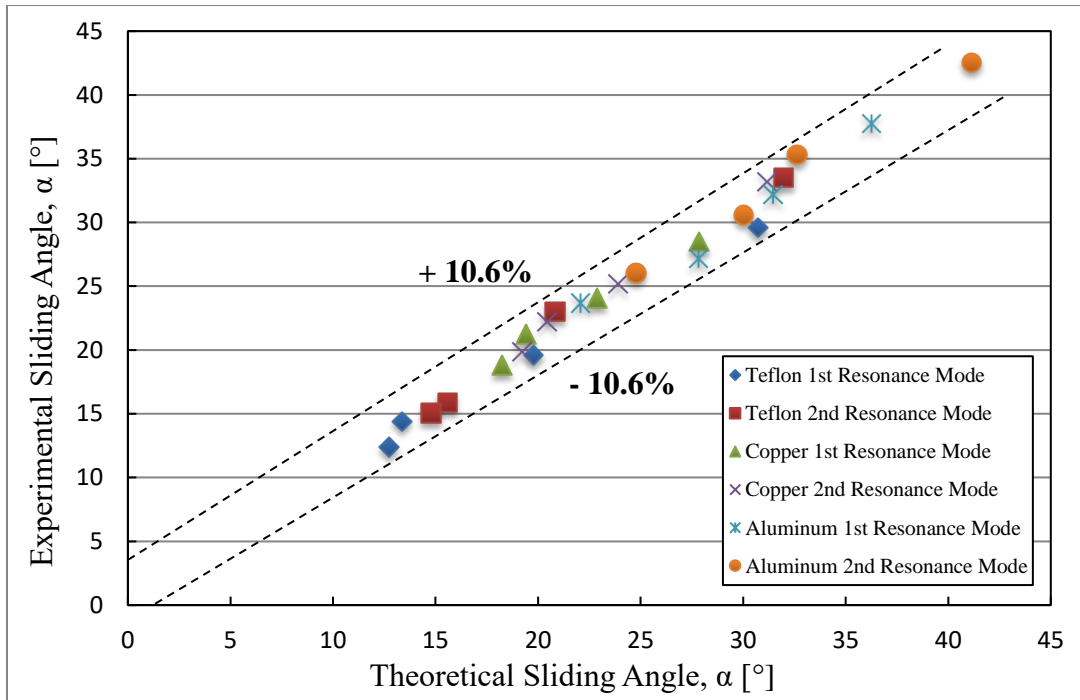


Fig. 5.10 Comparison between the theoretical and experimental sliding angle

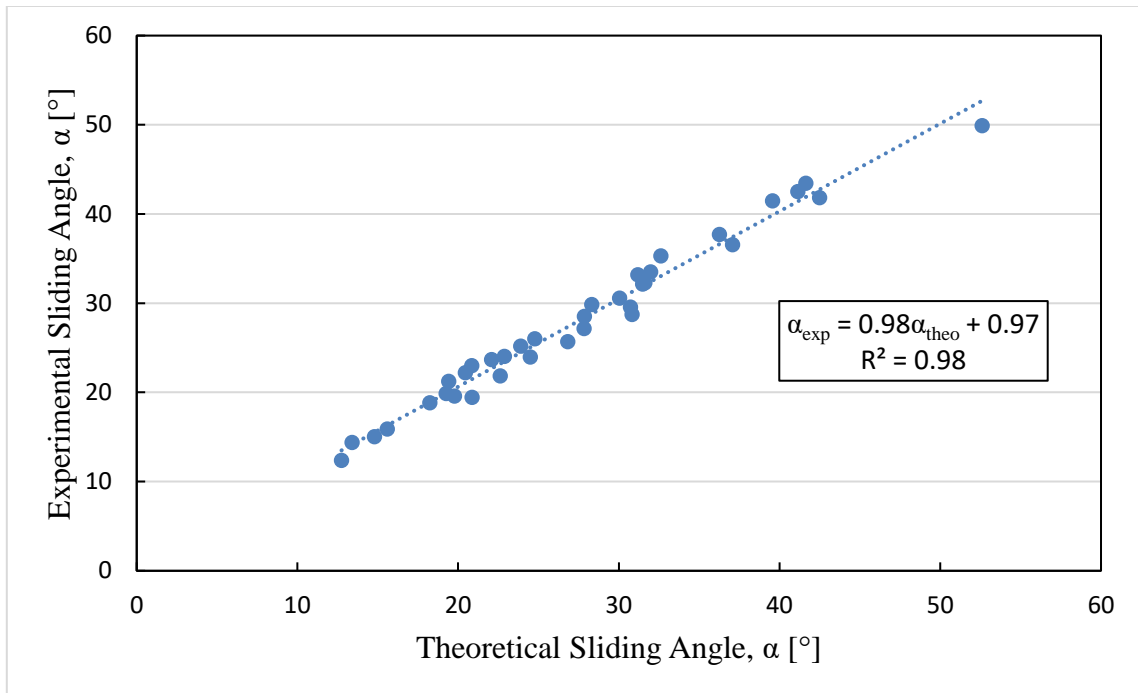


Fig. 5.11 Comparison in theoretical and experimental sliding angle with a R^2 of 0.98

5.4 Sliding angle enhancement comparison between the first and second resonance modes of vibration

When the first resonance mode of vibration is imposed, the droplet motion exhibits greater lateral motion, which helps overcome the energy barrier associated with surface tension. Based on analytical and experimental results in Tables 5.6 to 5.11, it is evident that the first resonance mode of vibrations is better in terms of sliding angle enhancement than the second resonance mode. Tables 5.12 through 5.14 show the experimental sliding angle results with and without the imposed of vibrations and it is evident that there is always an enhancement in sliding angle when imposing vibrations to the substrate.

Surface	Volume [μL]	Resonance Mode	$\alpha_{w/o \text{ vibrations}}$	$\alpha_{\text{vibrations}}$	$\alpha_{\text{exp. Enhancement}}$
Teflon	10	1 st	43.5°	29.6°	31.9%
		2 nd	43.5°	33.5°	22.9%
	20	1 st	29.9°	19.6°	34.4%
		2 nd	29.9°	23.0°	22.9%
	30	1 st	21.9°	14.4°	34.2%
		2 nd	21.9°	15.9°	27.3%
	40	1 st	19.5°	12.4°	36.4%
		2 nd	19.5°	15.0°	22.7%

Table 5.12 Sliding angle enhancement using a teflon surface

Surface	Volume [μL]	Resonance Mode	$\alpha_{w/o \text{ vibrations}}$	$\alpha_{\text{vibrations}}$	$\alpha_{\text{exp. Enhancement}}$
Copper	20	1 st	41.5°	28.5°	31.2%
		2 nd	41.5°	33.2°	20.0%
	30	1 st	32.3°	24.1°	25.5%
		2 nd	32.3°	25.2°	22.1%
	40	1 st	25.7°	21.3°	17.3%
		2 nd	25.7°	22.2°	13.6%
	50	1 st	24.0°	18.8°	21.4%
		2 nd	24.0°	19.9°	17.0%

Table 5.13 Sliding angle enhancement using a copper surface

Surface	Volume [μL]	Resonance Mode	$\alpha_{w/o \text{ vibrations}}$	$\alpha_{\text{vibrations}}$	$\alpha_{\text{exp. Enhancement}}$
Aluminum	20	1 st	49.9°	37.7°	24.4%
		2 nd	49.9°	42.5°	14.8%
	30	1 st	41.8°	32.2°	23.1%
		2 nd	41.8°	35.3°	15.6%
	40	1 st	36.6°	27.1°	25.8%
		2 nd	36.6°	30.6°	16.4%
	50	1 st	28.7°	23.7°	17.5%
		2 nd	28.7°	26.0°	9.4%

Table 5.14 Sliding angle enhancement using an aluminum surface

5.5 Condensation experiments results

The effects of vibrations on dropwise condensation with and without imposing acoustics on hydrophilic and hydrophobic surfaces have been studied. Experimental results show that acoustic stimuli have an effect on heat flux when using super-hydrophobic surfaces ($\theta > 140^\circ$). Contact angles on hydrophilic and hydrophobic surfaces were measured as shown in Table 4.1. Based on the results, the contact angle of droplets plays a significant role in condensation. In general, droplets with contact angle greater than 90° sheds faster and could lead to higher heat flux values. Previously, it has been shown that the lower contact angle hysteresis depicts higher heat flux [47]. Therefore, surface-droplet combinations that exhibit greater contact angle hysteresis are expected to show lower heat flux.

5.5.1 Heat transfer performance of standard surfaces

Several heat transfer experiments were performed to evaluate the effectiveness of the standard surfaces during condensation. The heat transfer experiments were performed by maintaining a relatively fixed humidity of moist-air (as described in Section 4.8) of $\phi = 71.8\%$ with a standard deviation of 2.7%. The data analysis of the condensation experiments is based on the measurement obtained from the HFS-4 integrated to the Peltier module. The average heat transfer coefficient was calculated, as follows:

$$h_{avg} = \frac{q''}{T_{amb} - T_s} \quad (42)$$

where q'' is the heat flux, T_{amb} is the ambient temperature inside the system, and T_s is the surface temperature of the material on the fluid side. Each experiment was performed for a total of 5 minutes after reaching steady state conditions for each distinctive surface temperature with and without imposing acoustic stimuli. Fig. 5.12 shows four different surfaces (aluminum, copper, hydro-copper, and painted metallic surface) that experienced dropwise condensation between 2 °C and 3 °C. From Fig. 5.12, approximate droplet size distribution statistical data (i.e. average and standard deviation) were obtained as shown in Table 5.15. Droplet distribution charts can be seen in Fig. 5.13.

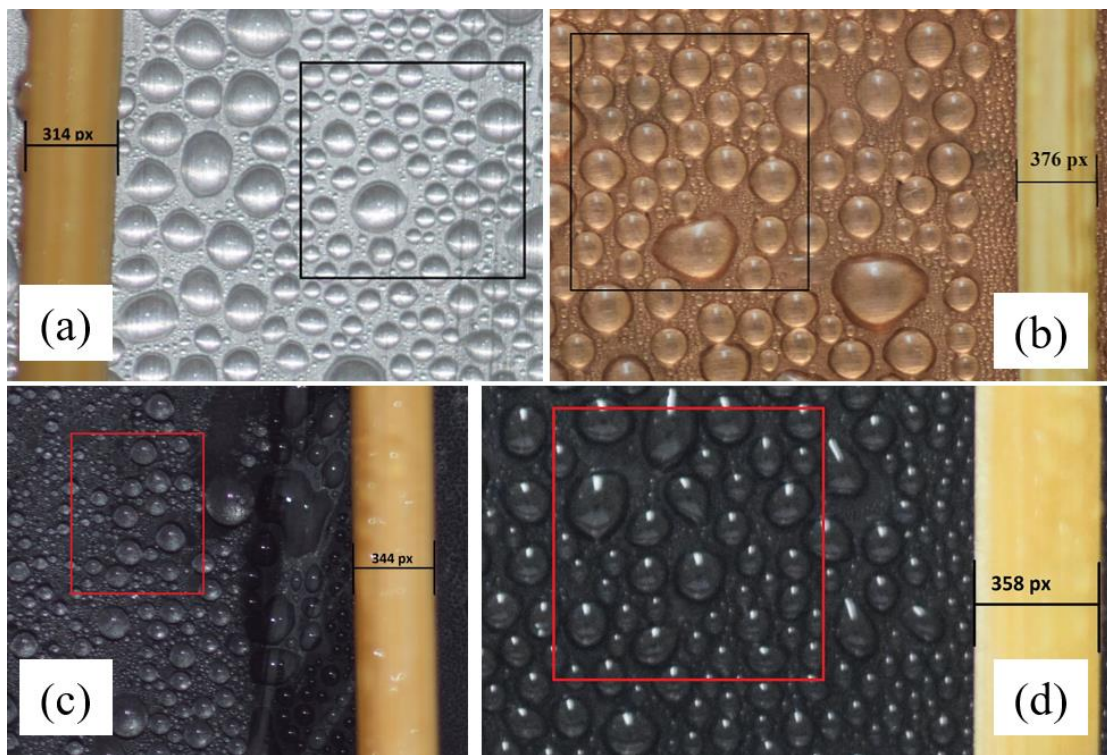


Fig. 5.12 Condensation droplet size of (a) aluminum at 2.8 °C, (b) copper at 2.2 °C, (c) hydro-copper at 2.9 °C, and (d) painted metallic surface at 2.6 °C

Surface	Static Contact Angle [θ]	Average Diameter [μm]	Median Diameter [μm]	Standard Deviation of Diameter [μm]	Average ¹ Volume [μL]
Aluminum	71°	1305	1237	469	0.31
Copper	81°	1496	1376	949	0.67
Hydro-Copper	153°	652	419	450	0.14
Painted Metallic	95°	1202	1138	445	0.51

Table 5.15 Droplet size distribution at an average surface temperature of 2.6 °C (Note¹: volume and other calculations can be found in Appendix A)

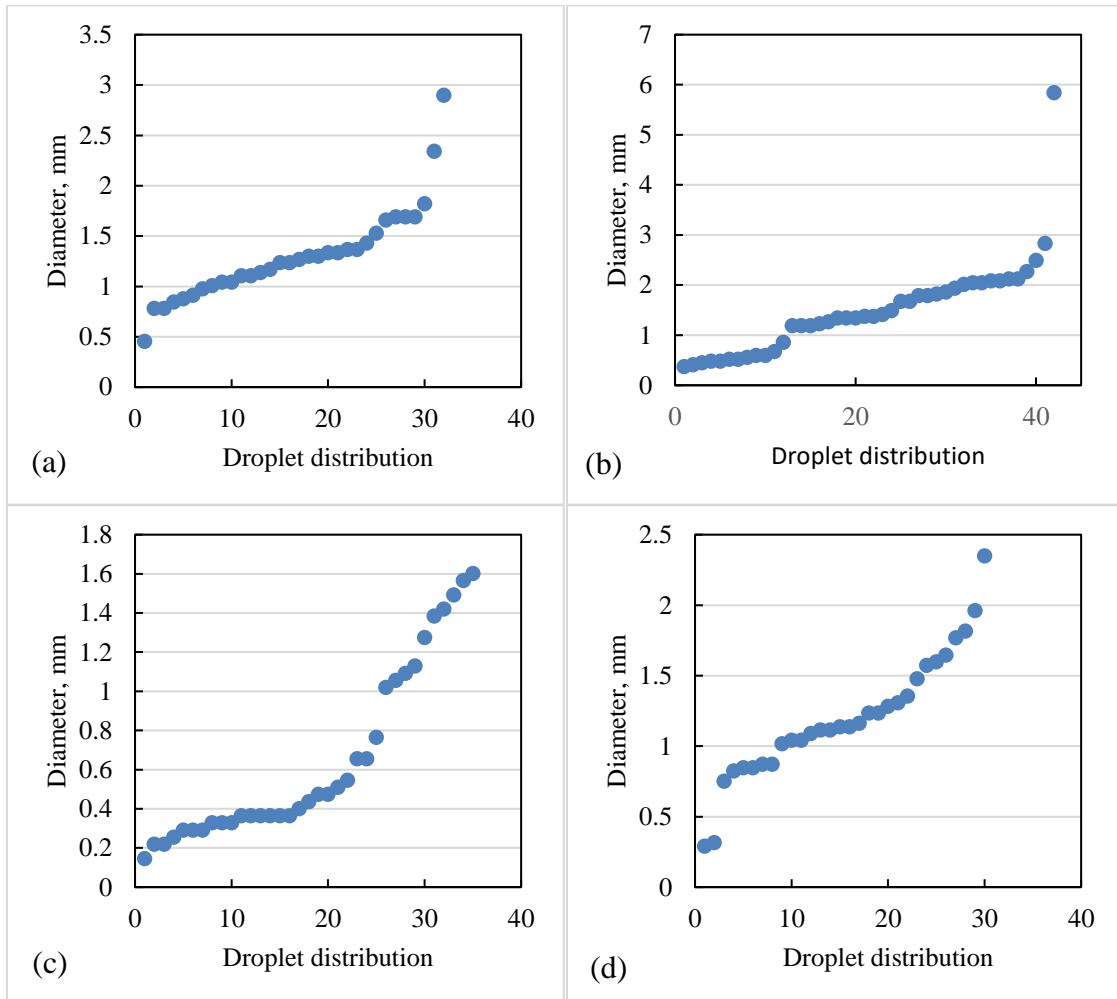


Fig. 5.13 Droplet size distribution of (a) aluminum, (b) copper, (c) hydro-copper, and (d) painted metallic surface

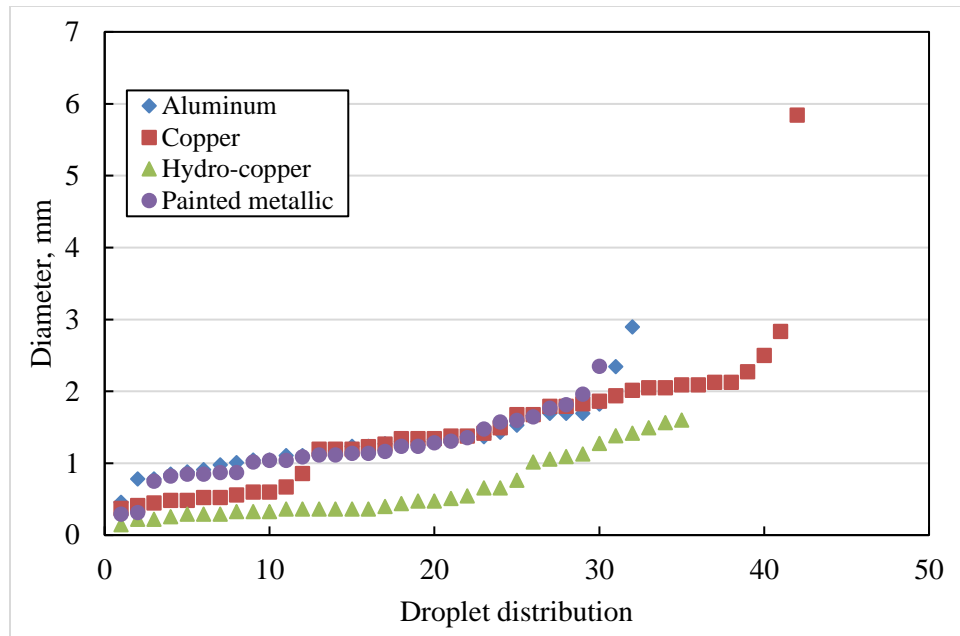


Fig. 5.14 Combined droplet size distribution for all surfaces

Fig. 5.13 and Fig. 5.14 show the droplet size distribution curves for all the corresponding surfaces. The curves show that droplet size varies depending on surface type and most of the droplet distributions match each other in the range of 1 mm to 2 mm, except for hydro-copper surface. Appendix A shows the droplet distribution analysis based on contact area, surface area for the vapor side, and droplet height. Based on the data shown in Appendix A, copper and painted metallic surfaces depict higher droplet surface area for the vapor side, which facilitates the droplet growth process. However, the aluminum surface shows lower droplet surface area for the vapor side, which should lead to lower heat transfer rate. Moreover, the hydro-copper surface depicts the lowest droplet surface area for the vapor side, which explains why it has the lowest heat transfer rate than the other surfaces during condensation, as seen below.

To understand the effects of condensation heat transfer within distinctive surfaces, a comprehensive condensation study was conducted. Tables 16 through 19 show different parameters used for condensation such as ambient temperature, surface temperature, moist-air humidity ratio, heat flux, and temperature gradient without the use of acoustic vibrations. Based on the results, copper depicts higher heat flux rates whereas hydro-copper shows the lowest heat flux rates. Low heat flux rates for hydro-copper have been observed despite of its good wetting properties. One of the main reasons for low heat flux rate is due to the fact that the surface area on the vapor side is relatively large compared to the contact area that each droplet makes with the solid surface. As a result, it is expected that such a super-hydrophobic surface depicts higher thermal resistance for each individual droplet during its growth process. Moreover, a recent study revealed that thermal resistance has a direct effect on droplet growth on the surface, which affects the heat transfer rates [48]. The condensation experiments also show that surfaces with contact angles close to 90° show the greatest amount of heat rate when compared to surfaces with high or low contact angles. Fig. 5.14 shows that the copper surface has a wide distribution of droplets when compared to other surfaces. This in turn implies that dropwise condensation as heat transfer mode is more prevalent during the overall droplet growth process when copper is used when no vibrations is imposed.

In dropwise condensation, droplets are expected to slide from a vertical surface when the droplet diameter exceeds the capillary length and gravity overcomes the capillary force [9]. Therefore, when the droplet slides off from the surface, nucleation

sites become available, which results in greater condensate amount and better heat transfer.

Surface	Case	T_{amb} [°C]	T_s [°C]	Humidity Ratio [%]	q'' $\left[\frac{W}{cm^2}\right]$	ΔT [°C]
Copper	1	21.2	2.7	70.2	5.6	18.5
	2	21.8	4.0	65.8	4.9	17.8
	3	21.5	6.6	67.5	4.1	14.9
	4	21.2	8.6	68.7	3.3	12.6
	5	20.9	10.8	71.0	2.7	10.1
	6	20.5	12.7	72.8	2.0	7.8
	7	20.2	15.7	75.7	0.8	4.5

Table 5.16 Condensation results using a copper surface without imposing acoustic vibrations

Surface	Case	T_{amb} [°C]	T_s [°C]	Humidity Ratio [%]	q'' $\left[\frac{W}{cm^2}\right]$	ΔT [°C]
Aluminum	1	21.0	3.3	69.4	3.0	17.7
	2	21.2	4.8	68.6	2.9	16.4
	3	21.2	6.9	73.9	2.6	14.3
	4	21.2	8.7	74.3	2.1	12.5
	5	20.9	10.3	75.4	1.8	10.6
	6	20.9	12.0	75.1	1.5	8.9
	7	20.7	14.2	76.9	0.8	6.5

Table 5.17 Condensation results using an aluminum surface without imposing acoustic vibrations

Surface	Case	T_{amb} [°C]	T_s [°C]	Humidity Ratio [%]	q'' [$\frac{W}{cm^2}$]	ΔT [°C]
Hydro-Copper	1	20.9	2.9	73.2	2.4	18.0
	2	21.5	4.2	72.1	2.1	17.3
	3	21.5	6.4	72.5	1.8	15.1
	4	21.3	8.3	76.8	1.5	13.0
	5	21.1	10.1	75.4	1.2	11.0
	6	21.0	11.9	77.0	0.9	9.1
	7	20.8	13.8	77.6	0.7	7.0

Table 5.18 Condensation results using a hydro-copper surface without imposing acoustic vibrations

Surface	Case	T_{amb} [°C]	T_s [°C]	Humidity Ratio [%]	q'' [$\frac{W}{cm^2}$]	ΔT [°C]
Painted Metallic	1	21.3	3.4	72.0	3.9	17.9
	2	21.1	4.9	72.4	3.5	16.2
	3	20.7	6.8	74.3	3.0	13.9
	4	20.6	8.2	76.0	2.4	12.4
	5	20.4	9.7	76.5	1.8	10.7
	6	20.1	11.8	72.2	1.6	8.3
	7	19.7	14.5	73.9	1.0	5.2

Table 5.19 Condensation results using a painted metallic surface without imposing acoustic vibrations

The results from Tables 5.16 to 5.19 are illustrated in terms of temperature difference ($\Delta T = T_{amb} - T_s$) and heat flux, as shown in Fig. 5.15. The figure shows that the average droplet volume (see Table 5.15) has an effect on condensation rate. Moreover, the hydro-copper surface depicts the worst heat transfer performance of all the surfaces, which also contains a large number of small droplets on the surface.

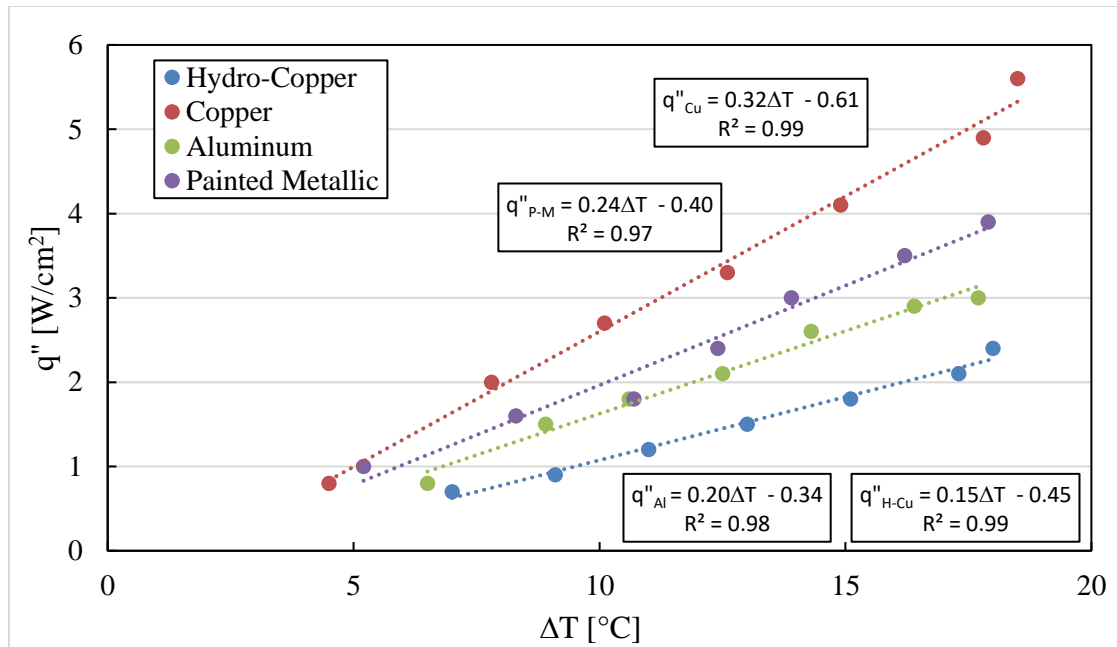


Fig. 5.15 Condensation heat flux curves for non-vibration cases

5.5.2 Heat transfer performance of standard surfaces with vibrations imposed

In dropwise condensation, the relationship between droplet size distribution and heat transfer plays a significant role in condensation [9] as discussed above. Migliaccio [9] observed that vibrations help reduce the population of large droplets, which leads to better heat transfer performance. Therefore, all the surfaces used in this study were subjected to acoustic vibrations. The excitation frequencies ranging from 20 Hz to 60 Hz were imposed to the system to determine any improvements in heat transfer rate. The induced vibration frequencies were initially calculated based on the Noblin's equation (Equation 13). The first resonant mode of vibrations were imposed because it leads to better droplet shedding as described in the droplet sliding section of this study. However, when imposing vibrations to the system with a frequency sweep, it appears that the hydrophilic surfaces showed less enhancement in terms of heat flux values when

compared to the super-hydrophobic surface (i.e. hydro-copper). Tables 21 through 24 show the results in terms of heat flux values and heat transfer enhancement under the effects of acoustic vibrations, when taking into account temperature difference and air temperature. The increase in heat transfer rate per unit area was calculated as follows [9]:

$$\eta = \frac{\hat{q}'' - q''}{q''} \times 100\% \quad (43)$$

where \hat{q}'' is the heat flux for the vibration cases and q'' is the stationary (no vibration) heat flux.

Although copper still performs the best in terms of heat flux even under the effects of acoustics, the heat transfer enhancement values were not as significant when compared to the super-hydrophobic surface. The heat flux enhancement, η , for the hydrophilic surfaces were relatively small; however, the super-hydrophobic surface depicts a significant enhancement in heat flux when imposing vibrations. One possible explanation for the minimal enhancement in heat transfer in the hydrophilic cases can be attributed to the effects of the resonant frequencies. Migliaccio [9] found that excitation frequencies within 100 to 200 Hz leads to a significant improvement in heat transfer rates of 70% when using a hydrophobic surface ($\theta = 114^\circ$). Celestini *et al.* derived an expression for estimating the vibration mode of submillimeter-size droplets [37] as shown in Chapter 2 (see Equation 17). Table 5.15 shows that the average droplet diameter for all surfaces were less than $r \sim 0.75$ mm, which can be characterized as a submillimeter-size droplets. Therefore, the use of the rocking mode frequency ω_0 , as

shown in Equation 17, can be applicable to estimate the vibration mode of submillimeter-size droplets [37]. Based on Celestini's *et al.* [37] developed oscillator model, the following frequencies for each surface were obtained as follows:

Surface	θ [°]	$h(\theta)$	R [mm]	ω_0 [Hz]
Copper	81	0.95	0.65	144
Aluminum	71	0.95	0.75	126
Hydro-copper	153	0.08	0.33	110
Painted Aluminum	95	0.8	0.60	139

Table 5.20 The simple oscillator expression to obtain the rocking mode excitation, ω_0 , values

where $h(\theta)$ is numerically computed and is dependent on wetting contact angle and obtained from Celestini *et al.* correlation chart [37]. Table 5.20 shows that excitation frequencies in the range of 100 and 200 Hz are ideal for heat transfer performance [9]. However, the existing system used in the study could be used reliably up to 60 Hz. In a future study, a more condensation system with a surface acoustic wave device capable of reaching frequencies of 200 Hz should be considered.

Based on the heat flux performance and heat transfer enhancement from Tables 5.21 to 5.24, the copper surface is the best performer, whereas the hydro-copper depicts the greatest enhancement in terms of heat flux (45% enhancement). It has been observed that the hydro-copper surface depicts the lowest performance due to its high contact angle and lowest contact area compared to the surface area in the vapor side when no vibrations are imposed. However, Fig. 5.16 shows that when imposing acoustics to the

system while using the hydro-copper surface, with a frequency sweep of 40 to 60 Hz, vibrations helped shed droplets rapidly, which allowed for new small droplets to nucleate. As a result, enhancements in heat transfer rates could be achieved when using the super-hydrophobic surface under the effects of imposed acoustic vibrations.

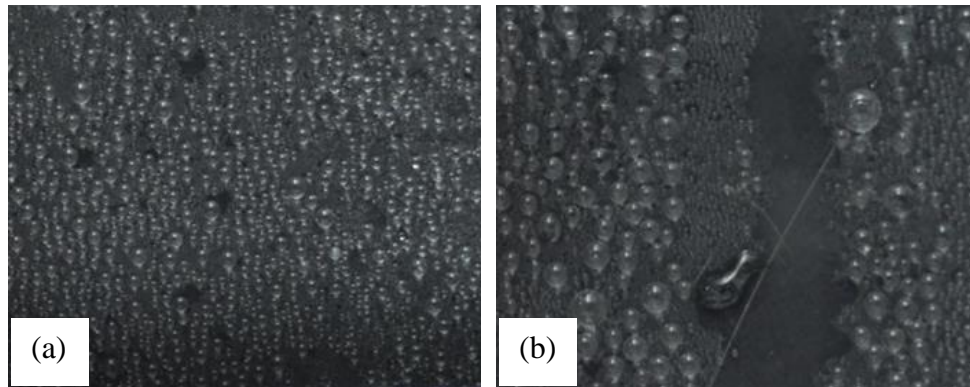


Fig. 5.16 Hydro-copper image analysis of (a) condensate droplets without the use of vibration and (b) condensate droplets with the use of vibrations that leads to a refreshed surface area for new droplet nucleation

Surface	Case	T_{amb} [°C]	T_s [°C]	Humidity Ratio [%]	q'' [$\frac{W}{cm^2}$]	ΔT [°C]	η
Copper with vibrations	1	22.0	2.7	61.5	5.7	19.3	2%
	2	21.4	3.8	62.6	5.2	17.6	6%
	3	21.1	6.7	64.2	4.4	14.4	7%
	4	21.1	8.4	65.5	3.9	12.7	18%
	5	20.8	10.6	67.3	2.9	10.2	7%
	6	20.5	12.5	69.1	2.2	8.0	10%
	7	20.1	15.3	70.8	0.9	4.8	13%

Table 5.21 Condensation results using a copper surface while imposing acoustic vibrations

Surface	Case	T_{amb} [°C]	T_s [°C]	Humidity Ratio [%]	q'' [$\frac{W}{cm^2}$]	ΔT [°C]	η
Aluminum with vibrations	1	21.6	3.2	64.8	3.1	18.4	3%
	2	21.3	5.2	67.2	2.9	16.1	0%
	3	20.7	6.8	66.5	2.5	13.9	-4%
	4	20.2	8.4	69.0	2.1	11.8	0%
	5	20.9	9.9	72.3	2.0	11.0	11%
	6	21.3	12.0	75.1	1.6	9.3	7%
	7	21.1	14.5	75.0	0.9	6.6	13%

Table 5.22 Condensation results using an aluminum surface while imposing acoustic vibrations

Surface	Case	T_{amb} [°C]	T_s [°C]	Humidity Ratio [%]	q'' [$\frac{W}{cm^2}$]	ΔT [°C]	η
Hydro- Copper with vibrations	1	21.0	2.9	68.4	3.4	18.1	45%
	2	20.7	4.6	71.7	2.9	16.1	34%
	3	21.7	6.3	72.9	2.6	15.4	43%
	4	21.1	8.3	73.0	2.0	12.8	39%
	5	21.2	10.1	74.3	1.7	11.1	39%
	6	21.0	11.8	71.6	1.3	9.2	35%
	7	20.7	14.0	72.7	0.7	6.7	15%

Table 5.23 Condensation results using a hydro-copper surface while imposing acoustic vibrations

Surface	Case	T_{amb} [°C]	T_s [°C]	Humidity Ratio [%]	q'' [$\frac{W}{cm^2}$]	ΔT [°C]	η
Painted Metallic with vibrations	1	21.2	3.2	72.2	4.0	18.0	3%
	2	21.1	5.1	72.5	3.6	16.0	3%
	3	20.6	6.5	74.8	3.1	14.1	3%
	4	20.6	7.9	75.6	2.7	12.7	13%
	5	20.4	9.6	76.3	2.2	10.8	22%
	6	20.0	11.8	72.4	1.7	8.2	6%
	7	19.7	14.4	74.3	1.1	5.3	10%

Table 5.24 Condensation results using a painted metallic surface while imposing acoustic vibrations

Fig. 5.17 to 5.20 depict heat flux values and heat transfer enhancement based on temperature difference for both stationary and imposed vibrations cases. The figures also show that the hydrophilic and hydrophobic surfaces show significant heat transfer enhancement when ΔT is between 10 to 15 °C. Furthermore, from Tables 5.21, 5.22 and 5.24, it is evident that the heat transfer enhancements due to imposed vibrations reach a maximum value in the ΔT range of 10 to 12.5 °C. It is known that when ΔT increases, the number of droplets on the condensing surface also increases [49]. It is suggested that when ΔT reaches 10 to 12.5 °C, there are sufficient droplets on the surface that have not experienced a significant level of droplet coalescence, which allows for a higher rate of droplet shedding when vibrations are imposed. It is also suggested that when ΔT is below the range for dropwise-to-filmwise transition as condensation mode, droplets can still shed without coalescing or forming a liquid film. Therefore, imposing acoustics frequencies on surfaces to enhance condensation should take into consideration ΔT as well as relative humidity [50]. In the case of the super-hydrophobic surface cases, vibrations led to enhancements in heat transfer for most ΔT values because of the high level of hydrophobicity, which minimizes droplet contact area. As a result, droplets on hydro-copper are less affected by surface tension effects, which in turn allow for a more effective shedding mechanism under the effects of vibration.

Fig. 5.21 to 5.24 show the condensation convective heat transfer curves and heat transfer coefficient enhancement. Based on experimental results, the greatest enhancement of h on hydrophilic and hydrophobic cases occur when ΔT is in the range of 10 °C – 13 °C with an average enhancement of approximate 13%. For the hydro-

copper, there is always an enhancement for most ΔT , but the highest enhancement occurs at ΔT of 18.1 °C with an h enhancement of 30.7%. Low h enhancements are found when ΔT is higher than 15 °C on hydrophilic and hydrophobic surfaces. This can be attributed to droplet coalescence and the onset of filmwise condensation or liquid film formation, which are less susceptible to the imposed acoustic resonant frequencies due to a decrease in the height of the vibration nodes within the larger droplets or streaks of liquid.

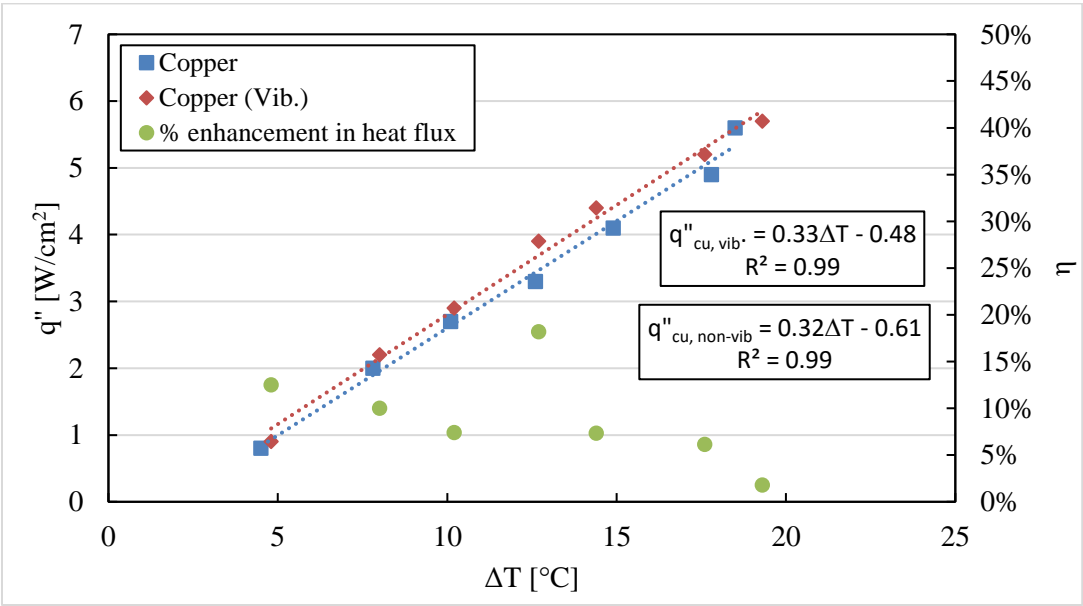


Fig. 5.17 Condensation heat flux curve comparison of copper with and without imposing vibrations to the system

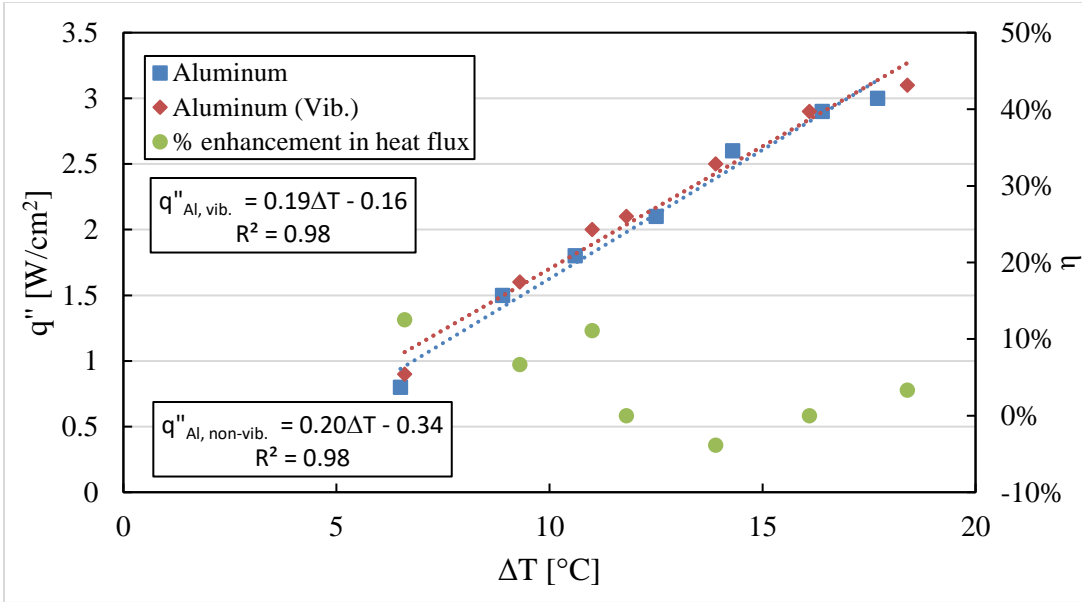


Fig. 5.18 Condensation heat flux curve comparison of aluminum with and without imposing vibrations to the system

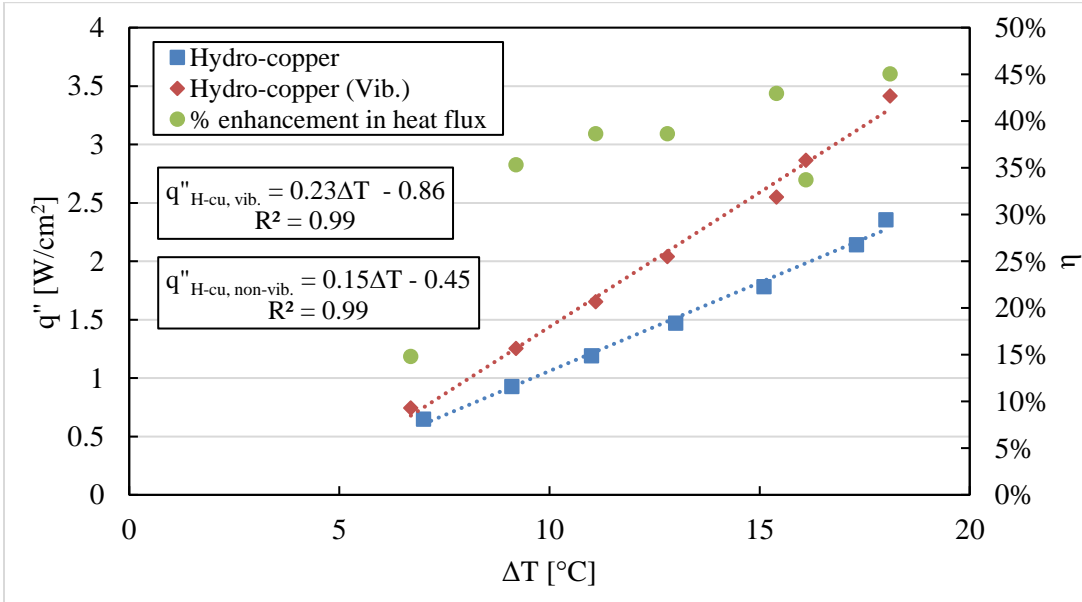


Fig. 5.19 Condensation heat flux curve comparison of hydro-copper with and without imposing vibrations to the system

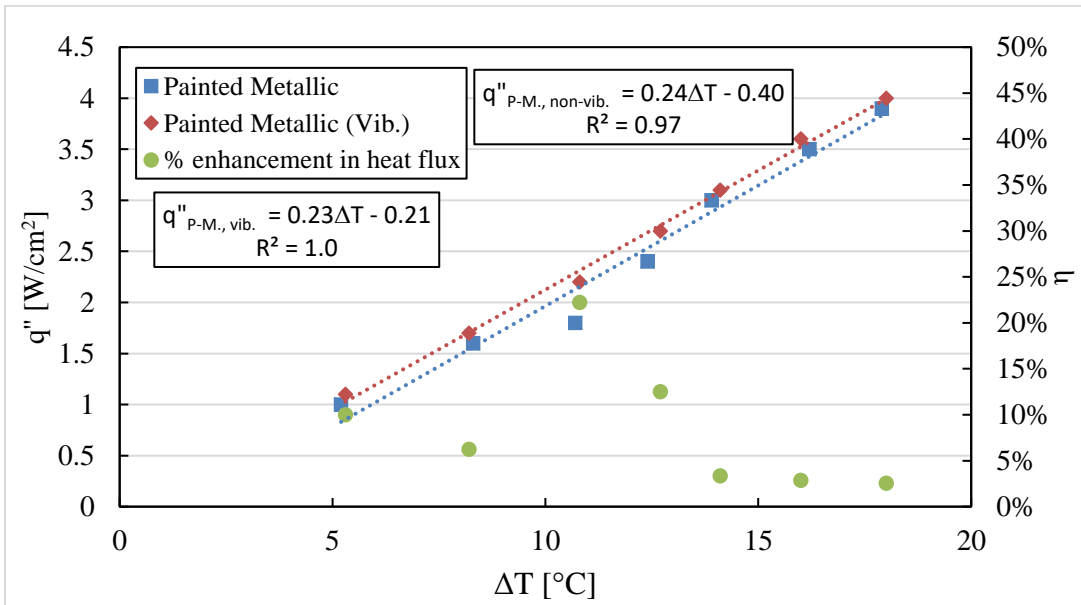


Fig. 5.20 Condensation heat flux curve comparison of a metallic surface with and without imposing vibrations to the system

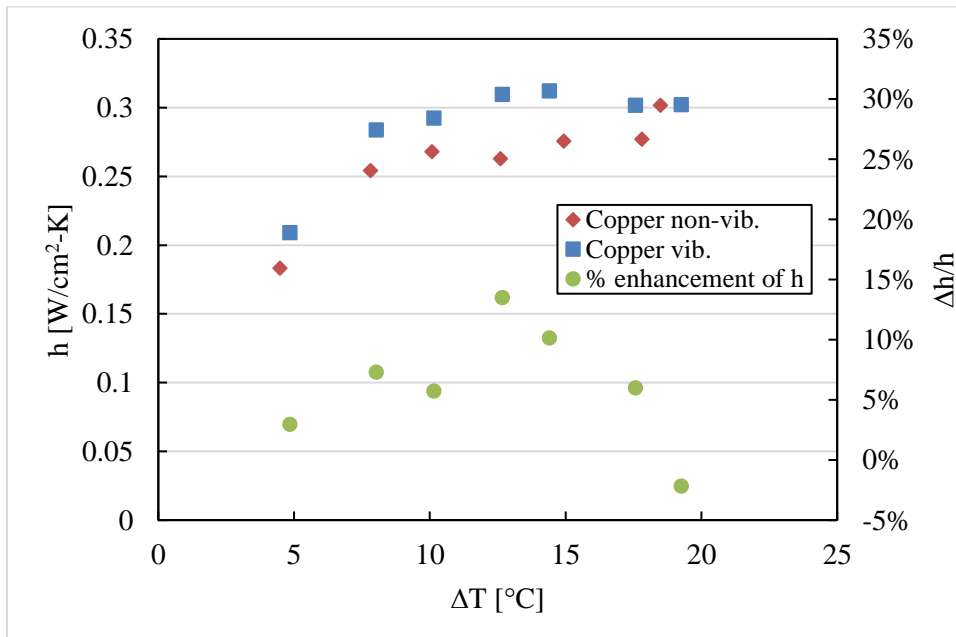


Fig. 5.21 Condensation convective heat transfer curve comparison of copper with and without imposing vibrations to the system

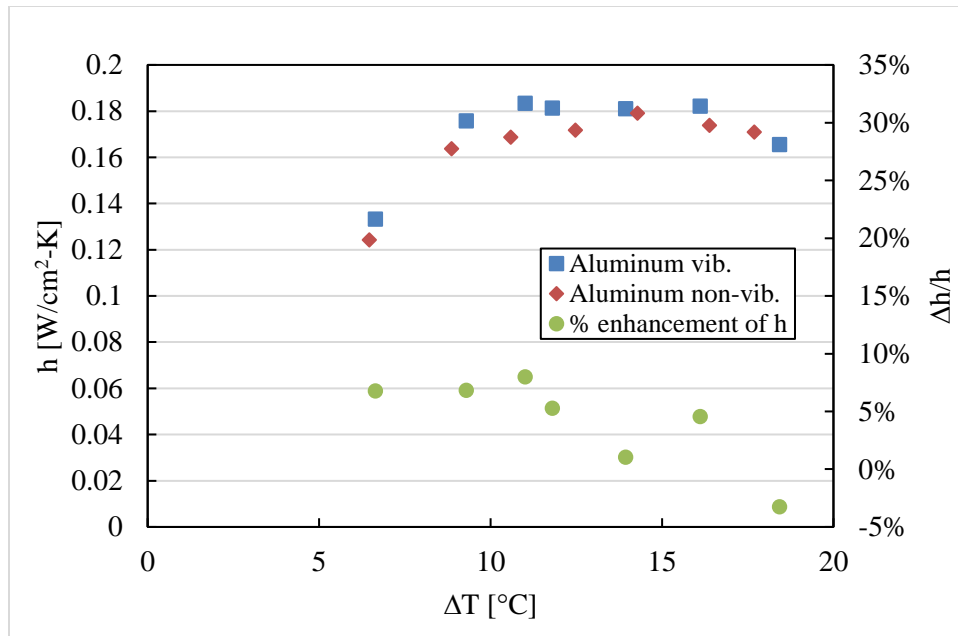


Fig. 5.22 Condensation convective heat transfer curve comparison of aluminum with and without imposing vibrations to the system

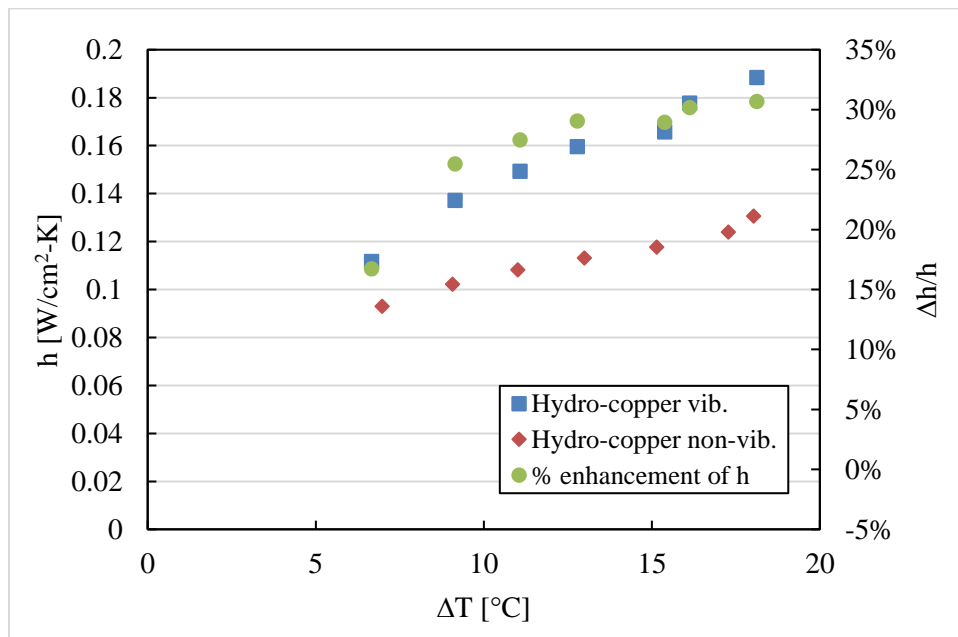


Fig. 5.23 Condensation convective heat transfer curve comparison of hydro-copper with and without imposing vibrations to the system

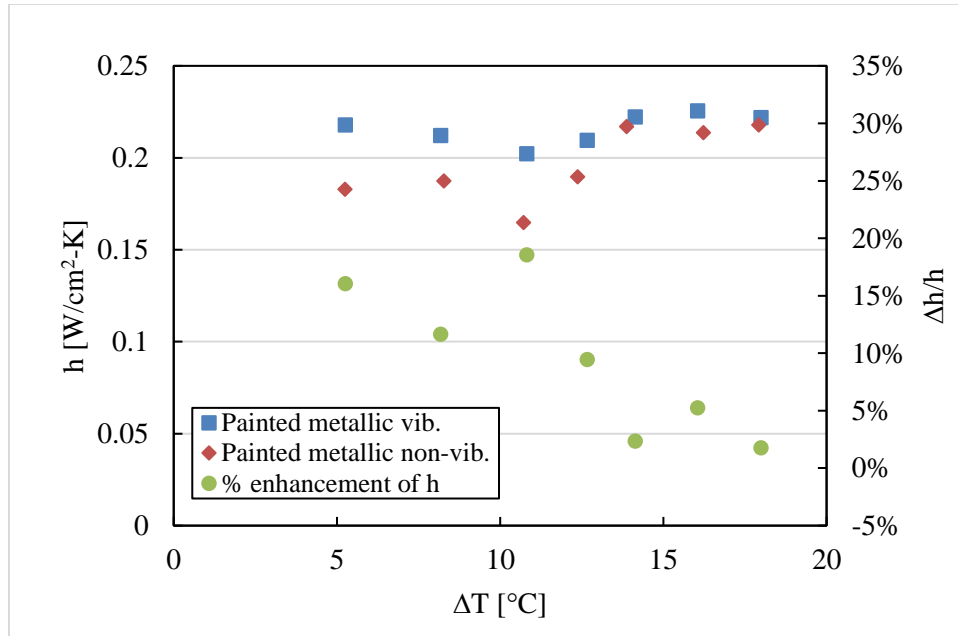


Fig. 5.24 Condensation convective heat transfer curve comparison of painted metallic surface with and without imposing vibrations to the system

5.5.3 Empirical heat transfer coefficient correlations

An empirical heat transfer coefficient correlation has been postulated for each hydrophobic and hydrophilic surface with and without the imposed of vibrations. The correlation was fitted by using the experimental data obtained during condensation. The ambient temperature difference and contact angles of droplets were set as independent variables. The convective heat transfer coefficient correlation for condensation was postulated as follows:

$$h = a \left(\cos \left(\theta - \frac{\pi}{2} \right) \right)^b (\phi_T)^c \quad (44)$$

where a, b, and c are determined from experimental data. The non-dimensional temperature difference, ϕ_T , is defined as:

$$\phi_T = \frac{T_d - T_s}{T_{amb} - T_s} \quad (45)$$

where T_d is the dew temperature, T_s is the surface temperature, and T_{amb} is the ambient temperature. Temperatures were obtained from experiments during condensation by using the humidity probe and thermocouples.

Based on experimental results and a regression analysis using experimental data, the empirical heat transfer coefficient correlations for hydrophilic surfaces ($\theta < 90^\circ$ or $\pi/2$) without the use of vibrations (Equation 46) and with vibrations (Equation 47) were postulated as follows:

$$h = 0.36 \left(\cos \left(\theta - \frac{\pi}{2} \right) \right)^{11.4} (\phi_T)^{0.26}, R^2 = 0.97 \quad (46)$$

$$h = 0.39 \left(\cos \left(\theta - \frac{\pi}{2} \right) \right)^{11.4} (\phi_T)^{0.32}, R^2 = 0.97 \quad (47)$$

In addition, another set of empirical heat transfer coefficient correlations for hydrophobic surfaces ($\theta > 90^\circ$ or $\pi/2$) without the use of vibrations (Equation 48) and with vibrations (Equation 49) were postulated as follows:

$$h = 0.23 \left(\cos \left(\theta - \frac{\pi}{2} \right) \right)^{0.69} (\phi_T)^{0.30}, R^2 = 0.95 \quad (48)$$

$$h = 0.26 \left(\cos \left(\theta - \frac{\pi}{2} \right) \right)^{0.41} (\phi_T)^{0.34}, R^2 = 0.85 \quad (49)$$

Since hydro-copper depicted an enhancement in terms of both heat flux and convective condensation heat transfer, another set of correlations without (Equation 50) and with (Equation 51) the effects of vibrations have been postulated as follows:

$$h = 0.32 \cos\left(\theta - \frac{\pi}{2}\right) (\phi_T)^{0.43}, R^2 = 0.95 \quad (50)$$

$$h = 0.49 \cos\left(\theta - \frac{\pi}{2}\right) (\phi_T)^{0.63}, R^2 = 0.99 \quad (51)$$

Based on the empirical correlations, it is evident that surface tension is a dominant mechanism on hydrophilic surfaces given the large magnitude of exponent b , see Equations 44, 46 and 47. Therefore, low imposed acoustic vibrations have a limited effect on condensation heat transfer rates on such surfaces. However, for the hydrophobic cases (Equations 48 and 49), the effects of surface tension and temperature on heat transfer are comparably significant. From Equations 50 and 51, it is evident that acoustic vibrations suppress surface tension effects given the greater magnitude of exponent c in Equation 51 when compared to Equation 50. Fig. 5.25 shows that the proposed correlations fit the experimental results well.

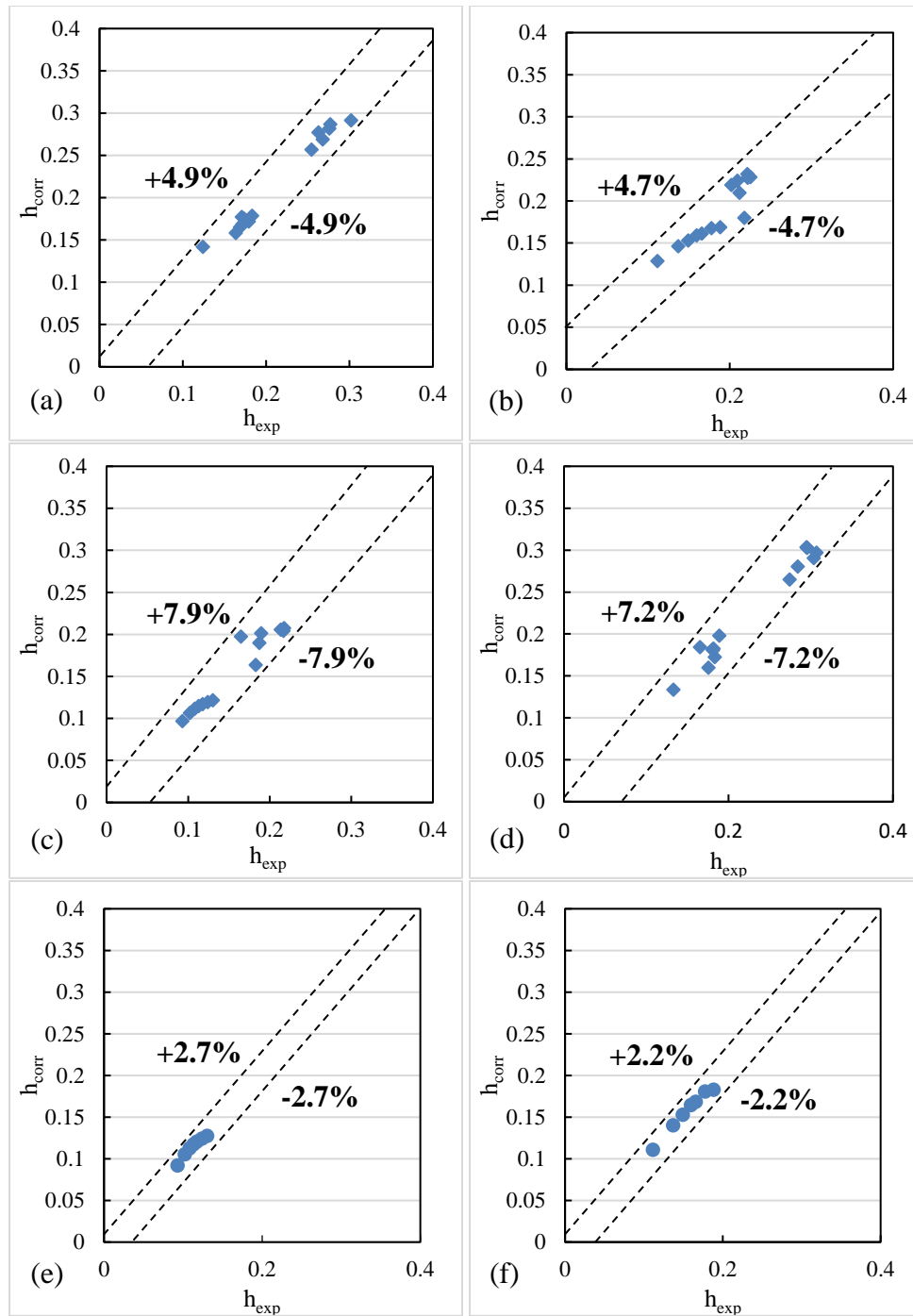


Fig. 5.25 Relative error of the developed correlations based on (a) hydrophilic surfaces ($\theta < 90^\circ$ or $\pi/2$) without vibrations, (b) hydrophilic surfaces with vibrations, (c) hydrophobic surfaces ($\theta > 90^\circ$ or $\pi/2$) without vibrations, (d) hydrophobic with vibrations, (e) hydro-copper correlation without vibrations, and (f) hydro-copper correlation with vibrations

6. CONCLUSION

This study investigated the effects of acoustics on sliding angle of droplet on different surfaces with distinctive wetting characteristics. The relationship between sliding angle and body forces such as gravity and acoustic streaming was studied and a physics-based mathematical model was developed that is capable of predicting the critical sliding angle of droplets with and without the imposed of vibrations. Experimental results show that larger droplets can overcome the energy barrier more than smaller droplets as the droplet diameter exceeds the capillary length, and the associated retentive force is inversely proportional to contact angle for the same droplet volume.

Recent studies demonstrate that droplet lateral resonant motion can be induced by low frequency acoustic stimuli. Therefore, the use of an acoustic stimuli lead to a better droplet lateral resonant motion, which helps overcome the energy barrier caused by the hysteresis effect that is associated with the retentive force. For such cases, a theoretical model was developed and validated that is capable of predicting droplet-sliding angle as a function of static contact angle, advancing and receding angles, and resonance modes of vibrations. The effects of resonant modes of vibrations were studied to understand the droplet resonant behavior that can predict and estimate better lateral droplet motion for droplet shedding.

In general, two forms of resonant modes of vibrations were imposed to the system, and it has been investigated that the droplet motion for the first resonant mode of vibrations depicted stronger lateral motion than the second resonant mode. When the

first resonant mode of vibration was imposed on an inclined plane, the droplet motion exhibited stronger lateral motion that allowed to overcome the energy barrier associated with surface tension. However, the second resonant mode of vibrations exhibited a continuously combined vertical-horizontal motion, which led to lower dynamic contact angle hysteresis. Hence, it has been shown that the first resonant mode of vibrations is more active and effective than the second resonant mode, which led to better sliding enhancement as the experimental results showed. Furthermore, the imposed vibration oscillation force facilitated droplet shedding at lower sliding angles. In addition, under the effects of the first resonant mode, the acoustic acceleration along the sliding plane was found to be inversely proportional to droplet volume for the hydrophilic cases.

Results to date also show that the developed model is in a good accordance with the experimental data with and without the use of acoustic vibrations. The results also indicate that the acoustic-based model can be used effectively to relate imposed resonant frequencies to critical sliding angle of droplets. Therefore, results indicate that the resonance frequencies lead to a reduction in sliding angles.

The effects of vibrations on dropwise condensation had been studied to determine enhancements in terms of heat flux and convective heat transfer coefficient with and without the use of vibrations. Based on results, it has been shown that copper depicts higher condensation heat flux rates whereas the hydro-copper depicted the lowest heat flux rates. The heat transfer results suggest that larger surface area on the vapor side relative to the droplet contact area leads to lower heat flux rates. Moreover, it has been observed that super-hydrophobic surface depicts higher thermal resistance due to the

small contact area between the droplet and the condensing surface. Experimental results demonstrate that acoustic stimuli do have a significant effect in condensation heat flux and convective heat transfer coefficient when using a super-hydrophobic surface. A frequency sweep allowed droplets to shed faster, which in turn allowed small droplets to nucleate on the super-hydrophobic surface. Therefore, the use of vibrations for droplets with high contact angles helped reduce the population of large thermally inefficient droplets, which improved the heat transfer rate. In addition, based on experimental results, empirical correlations for dropwise condensation under the effects of acoustic streaming on hydrophilic and hydrophobic cases were developed and experimentally validated. The correlations show good agreement with experimental results.

Currently, little is known about the effects of acoustics on droplet shedding in condensation systems. Better condensers are needed in a host of applications, including water harvesting and desalination systems around the world where sustainability is a serious concern. Furthermore, their footprint and associated energy cost should be reduced to enable better use of resources. Therefore, by applying the adequate resonant mode, during the condensation process, the acoustically resonant surface may minimize film-wise condensation under the effects of resonant acoustic vibrations.

7. FUTURE WORK

Results indicate a relationship between acoustic stimuli and droplet shedding during dropwise condensation. The effects of acoustic stimuli during the dropwise condensation stages, including droplet nucleation, droplet growth and coalescence, should be evaluated under different conditions. Engineered surfaces, with distinct hydrophobic-hydrophilic patterns, should be designed to enable nucleation and growth, while promoting low-energy resonant droplet behavior to imposed acoustic stimuli, necessary for effective droplet shedding. A recent study demonstrated improvements in heat transfer rates when imposing relative large excitation frequencies, between 100 to 200 Hz. Therefore, a more complex condensation system should be fabricated with the capability to induce vibration frequencies as high as 200 Hz. The use of a piezoelectric actuator attached next to condensing surface may facilitate droplet shedding and enhance condensation heat transfer rates. The use of a surface acoustic wave (SAW) motion, capable of vibrating the surface along the sliding plane may facilitate droplet shedding and improve the condensation energy efficiency and heat transfer performance. In addition, a lab-scale condenser consisting of self-vibrating tubes, should be fabricated and characterized to evaluate the effectiveness of flow-induced low frequency vibrations on condensation heat transfer rates.

REFERENCES

- [1] Schmidt, E., W. Schurig, and W. Sellschopp. "Versuche über die Kondensation von Wasserdampf in Film-und Tropfenform." *Technische Mechanik und Thermodynamik* 1.2 (1930): 53-63.
- [2] Baudoin, M., Brunet, P., Bou Matar, O., and Herth, E. "Low power sessile droplets actuation via modulated surface acoustic waves." *Applied Physics Letters* 100.15 (2012): 154102.
- [3] Rose, J. W. "Dropwise condensation theory and experiment: a review." *Proceedings of the Institution of Mechanical Engineers, Part A: Journal of Power and Energy* 216.2 (2002): 115-128.
- [4] Fürstner, R., Barthlott, W., Neinhuis, C., and Walzel, P. "Wetting and self-cleaning properties of artificial superhydrophobic surfaces." *Langmuir* 21.3 (2005): 956-961.
- [5] Yao, C., Ph.D. Dissertation: "Study of the Effects of Surface Morphology and Droplet Growth Dynamics on Condensation Heat Transfer," Doctor of Philosophy in Mechanical Engineering, Texas A&M University, 2013.
- [6] Lai, Chen-Ling, "Effects of Induced Acoustics Vibrations on Droplet Shedding on Hybrid Micro-Structured Surfaces," Master of Science in Mechanical Engineering, May 2014, Texas A&M University.

- [7] Mejia, J.E., J. Alvarado, C.W. Yao, "Effects of acoustics on induced droplet shedding for dropwise condensation." *Bulletin of the American Physical Society*, Vol. 61, 2016.
- [8] Miljkovic, Nenad, and Evelyn N. Wang. "Condensation heat transfer on superhydrophobic surfaces." *MRS Bulletin* 38.5 (2013): 397-406.
- [9] Migliaccio, Christopher P. "Resonance-induced condensate shedding for high-efficiency heat transfer." *International Journal of Heat and Mass Transfer* 79 (2014): 720-726.
- [10] Noblin, X., A. Buguin, and F. Brochard-Wyart. "Vibrated sessile drops: Transition between pinned and mobile contact line oscillations." *The European Physical Journal E: Soft Matter and Biological Physics* 14.4 (2004): 395-404.
- [11] Santos, M. J., S. Velasco, and J. A. White. "Simulation analysis of contact angles and retention forces of liquid drops on inclined surfaces." *Langmuir* 28.32 (2012): 11819-11826.
- [12] Furmidge, C. G. L. "Studies at phase interfaces. I. The sliding of liquid drops on solid surfaces and a theory for spray retention." *Journal of Colloid Science* 17.4 (1962): 309-324.
- [13] Good, Robert J. "Contact angle, wetting, and adhesion: a critical review." *Journal of Adhesion Science and Technology* 6.12 (1992): 1269-1302.
- [14] Yao, C. W., Garvin, T. P., Alvarado, J. L., Jacobi, A. M., and Jones, B.G. "Droplet contact angle behavior on a hybrid surface with hydrophobic and hydrophilic properties." *Applied Physics Letters* 101.11 (2012): 111605.

- [15] Bommer, S., Hagen S., Ralf S., Krishan K., Vivek S., and Nishith V. "Depinning of drops on inclined smooth and topographic surfaces: experimental and lattice Boltzmann model study." *Langmuir* 30.37 (2014): 11086-11095.
- [16] Cheng, K., Naccarato, B., Kim, K. J., and Kumar, A. "Theoretical consideration of contact angle hysteresis using surface-energy-minimization methods." *International Journal of Heat and Mass Transfer* 102 (2016): 154-161.
- [17] Meiron, Tammar S., Abraham Marmur, and I. Sam Saguy. "Contact angle measurement on rough surfaces." *Journal of Colloid and Interface Science* 274.2 (2004): 637-644.
- [18] Gao, Lichao, and Thomas J. McCarthy. "Contact angle hysteresis explained." *Langmuir* 22.14 (2006): 6234-6237.
- [19] Eral, H. B., and J. M. Oh. "Contact angle hysteresis: a review of fundamentals and applications." *Colloid and Polymer Science* 291.2 (2013): 247-260.
- [20] Albenge, O., Lacabanne, C., Beguin, J., Koënen, A., and Evo, C. "Experimental procedure to measure the blocking energy of liquid on smooth hydrophobic surfaces." *Langmuir* 18.23 (2002): 8929-8932.
- [21] Daniel, S., Sircar, S., Gliem, J., and Chaudhury, M. K. "Ratcheting motion of liquid drops on gradient surfaces." *Langmuir* 20.10 (2004): 4085-4092.
- [22] Brunet, P., J. Eggers, and R. D. Deegan. "Vibration-induced climbing of drops." *Physical Review Letters* 99.14 (2007): 144501.

- [23] Andersen, Nis Korsgaard, and Rafael Taboryski. "Drop shape analysis for determination of dynamic contact angles by double sided elliptical fitting method." *Measurement Science and Technology* 28.4 (2017): 047003.
- [24] Quéré, David, Marie-José Azzopardi, and Laurent Delattre. "Drops at rest on a tilted plane." *Langmuir* 14.8 (1998): 2213-2216.
- [25] Ruiz-Cabello, FJ Montes, M. A. Rodriguez-Valverde, and M. Cabrerizo-Vilchez. "A new method for evaluating the most stable contact angle using tilting plate experiments." *Soft Matter* 7.21 (2011): 10457-10461.
- [26] Frenkel, Yakovich Ilich. "On the behavior of liquid drops on a solid surface. 1. The sliding of drops on an inclined surface." *J. Exptl. Theoret. Phys. (USSR)*, 18, 659, 1948.
- [27] Extrand, Charles W., and Y. Kumagai. "Liquid drops on an inclined plane: the relation between contact angles, drop shape, and retentive force." *Journal of Colloid and Interface Science* 170.2 (1995): 515-521.
- [28] ElSherbini, A. I., and A. M. Jacobi. "Retention forces and contact angles for critical liquid drops on non-horizontal surfaces." *Journal of Colloid and Interface Science* 299.2 (2006): 841-849.
- [29] Extrand, C. W., and A. N. Gent. "Retention of liquid drops by solid surfaces." *Journal of Colloid and Interface Science* 138.2 (1990): 431-442.
- [30] Chow, Robert Tao-Ping. "On the ability of drops or bubbles to stick to non-horizontal surfaces of solids." *Journal of Fluid Mechanics* 137 (1983): 1-29.

- [31] Perez, M., Brechet, Y., Salvo, L., Papoular, M., and Suery, M. "Oscillation of liquid drops under gravity: Influence of shape on the resonance frequency." *EPL (Europhysics Letters)* 47.2 (1999): 189.
- [32] Lamb, Horace. *Hydrodynamics*. Cambridge university press, 1932.
- [33] Manor, Ofer. "Diminution of contact angle hysteresis under the influence of an oscillating force." *Langmuir* 30.23 (2014): 6841-6845.
- [34] Decker, E. L., and S. Garoff. "Using vibrational noise to probe energy barriers producing contact angle hysteresis." *Langmuir* 12.8 (1996): 2100-2110.
- [35] Sartori, P., Quagliati, D., Varagnolo, S., Pierno, M., Mistura, G., Magaletti, F., and Casciola, C. M. "Drop motion induced by vertical vibrations." *New Journal of Physics* 17.11 (2015): 113017.
- [36] Boreyko, Jonathan B., and Chuan-Hua Chen. "Restoring superhydrophobicity of lotus leaves with vibration-induced dewetting." *Physical Review Letters* 103.17 (2009): 174502.
- [37] Celestini, F., and Kofman, R. "Vibration of submillimeter-size supported droplets." *Physical Review E* 73.4 (2006): 041602.
- [38] Daniel, Susan, Manoj K. Chaudhury, and John C. Chen. "Fast drop movements resulting from the phase change on a gradient surface." *Science* 291.5504 (2001): 633-636.
- [39] Kim, Sunwoo, and Kwang J. Kim. "Dropwise condensation modeling suitable for superhydrophobic surfaces." *Journal of Heat Transfer* 133.8 (2011): 081502.

- [40] Neumann, A. W., A. H. Abdelmessih, and A. Hameed. "The role of contact angles and contact angle hysteresis in dropwise condensation heat transfer." *International Journal of Heat and Mass Transfer* 21.7 (1978): 947-953.
- [41] Le Fevre, E. J., and J. W. Rose. "An experimental study of heat transfer by dropwise condensation." *International Journal of Heat and Mass Transfer* 8.8 (1965): 1117-1133.
- [42] Industries, Adafruit. "Peltier Thermo-Electric Cooler Module + Heatsink Assembly – 12V 5A." *Adafruit Industries Blog RSS*.
- [43] Inc., Total Temperature Instrumentation. "Fuji Electric PXR4 Temperature Controller." *Temperature Controllers / Instrumart*.
- [44] "Pureguardian H8000B 120-Hour Elite Smart Mist Digital Ultrasonic Humidifier with Extendable Wand." *Walmart.com*.
- [45] Pierce, E., F. J. Carmona, and A. Amirfazli. "Understanding of sliding and contact angle results in tilted plate experiments." *Colloids and Surfaces A: Physicochemical and Engineering Aspects* 323.1 (2008): 73-82.
- [46] Yao, C. W., Lai, C. L., Alvarado, J. L., Zhou, J., Aung, K. T., and Mejia, J. E. "Experimental study on effect of surface vibration on micro textured surfaces with hydrophobic and hydrophilic materials." *Applied Surface Science* 412 (2017): 45-51.
- [47] Neumann, A. W., A. H. Abdelmessih, and A. Hameed. "The role of contact angles and contact angle hysteresis in dropwise condensation heat transfer." *International Journal of Heat and Mass Transfer* 21.7 (1978): 947-953.

- [48] Abu-Orabi, Mousa. "Modeling of heat transfer in dropwise condensation." *International Journal of Heat and Mass Transfer* 41.1 (1998): 81-87.
- [49] Maa, Jer Ru. "Drop size distribution and heat flux of dropwise condensation." *The Chemical Engineering Journal* 16.3 (1978): 171-176.
- [50] Castillo, Julian E., Justin A. Weibel, and Suresh V. Garimella. "The effect of relative humidity on dropwise condensation dynamics." *International Journal of Heat and Mass Transfer* 80 (2015): 759-766.
- [51] Olin, P., Lindström, S. B., Pettersson, T., & Wågberg, L. (2013). "Water drop friction on superhydrophobic surfaces." *Langmuir*, 29(29), 9079-9089.

APPENDIX A

A.1 Effects of friction on viscous dissipation in sliding droplet

The following demonstrates that friction force in the droplet sliding angle governing equation due to the viscous dissipation is not governed by bulk (macroscopic flow) fluid motion within each droplet. Olin *et al.* [51] developed an equation to determine the viscous dissipation of water droplets as follows:

$$\dot{Q}_V = \eta \int_{\Omega} (\nabla \vec{u})^2 dV \quad (\text{A-1})$$

where \vec{u} is the velocity field of the droplet and Ω is the interior of the droplet. A simplified version of the viscous dissipation equation (A-1) is as follows:

$$\dot{Q}_V \sim \eta \left(\frac{\dot{S}}{R} \right) r^3 = \eta R \dot{S}^2 \text{Bo}^{2/3} \quad (\text{A-2})$$

According to calculations, see Table A.1, \dot{Q}_V ranges from 4.39E-12 and 3.14E-09, which yields to very small numbers, almost approaching 0. Therefore, it can be assumed that $F_{\text{vis}} \cong 0$ due to dissipation associated with the macroscopic flow of fluid within each droplet. In addition, Table A.1 shows that the product of Capillary (Ca) and Bond (Bo) numbers (Ca·Bo) is very small, which suggests that the viscous dissipation mechanism (due to friction) is mainly dominated by the pinning-depinning process [51].

Furthermore, it is assumed that surface tension is more dominant than the viscous force effects. Moreover, another interpretation for the frictional force [51] was developed as follows,

$$F = b_{sh}Bo^{-1/2}mg \quad (A-3)$$

Given the expected low value of b_{sh} (~ 0.01) for hydrophilic and hydrophobic surfaces [51], the corresponding friction force would be much smaller than the surface tension and gravity force effects.

Velocity, v (m/s)	Dynamic Viscosity, μ (N·s/m ²)	Surface Tension, γ (N/m)	Density, ρ (kg/m ³)	Radius, R (m)	Ca	Bo	Ca·Bo
2.5E-03	8.91E-04	0.072	998	0.0016	3.09E-05	0.3	1.08E-05
6.7E-04	8.91E-04	0.072	998	0.0036	8.29E-06	1.8	1.46E-05

Table A.1 Physical properties of liquid droplets

A.2 Physical properties of droplets for condensation analysis

The following demonstrate the calculation used to estimate droplet contact radius, droplet size volume, droplet contact area, droplet height and surface area on the vapor side of a typical droplet. The droplet schematic below was used to estimate the average droplet size distribution and the other droplet characteristics, during dropwise condensation.

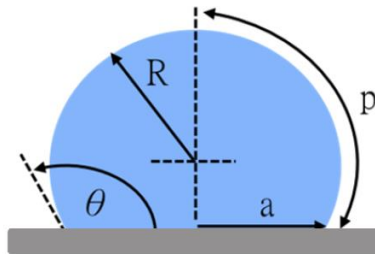


Fig. A.1 Typical droplet in dropwise condensation

a was used to determine the average droplet contact radius distributions by measuring and converting R , as follows:

$$a = R \sin \theta \quad (\text{A-4})$$

The average volume of the droplets was calculated by knowing the droplet contact angle and the average droplet radius based on image analysis, as follows:

$$V = \frac{\pi}{3} R^3 (2 + \cos \theta)(1 - \cos \theta)^2 \quad (\text{A-5})$$

The following was used to determine the average contact area of the droplet on the surface,

$$CA = \pi a^2 \quad (\text{A-6})$$

and the height of the average droplet was calculated as follows,

$$h = a \tan \theta \quad (\text{A-7})$$

The surface area on the fluid side was determined as follows,

$$SA = 2\pi R h \quad (\text{A-8})$$

Surface	θ [$^{\circ}$]	a [μm]	Vol_{min} [μL]	Vol_{max} [μL]	CA [m^2]	CA/V [1/m]	h [m]	$\sin(\theta)$ [rad]	SA_{vapor} [m^2]	SA/V [1/m]
Aluminum	71	851	0.081	0.8	2.27E-06	2817.2	2.50E-03	0.95	1.40E-05	1.70E+04
Copper	81	814.8	0.033	2.9	2.09E-06	2311.7	5.10E-03	0.99	2.70E-05	3.00E+04
Hydro-copper	153	163.7	0.004	0.7	8.41E-08	432.5	8.30E-05	0.45	1.90E-07	9.70E+02
Painted metallic	95	831.8	0.128	1.3	2.17E-06	1577.1	9.50E-03	1	5.00E-05	3.60E+04

Table A.2 Condensed droplet characteristics based on droplet contact radius, contact area, height, and surface area on the fluid side

A.3 Sliding droplet data for silicon wafer (SiO₂) surface case

The following tables show additional experimental data used to validate the sliding angle equations (Equations 33 and 40) when using a SiO₂ surface, with a contact angle of 77°. Tables A.3 through A.5 show good accordance between the theoretical and experimental values. Fig. 2.A shows the sliding enhancement when imposing the 1st and 2nd resonance mode of vibrations.

Surface	Volume [μL]	θ_{adv}	θ_{rec}	$\Delta\theta$	k	α_{theo}	α_{exp}	Error
SiO ₂ $\theta = 77^\circ$	20	91.5°	61.6°	29.9°	1.4	39.1°	39.0°	0.3%
	30	94.9°	59.6°	35.3°	1.4	33.3°	32.5°	2.7%
	40	95.7°	58.4°	37.3°	1.3	27.3°	26.6°	2.6%
	50	96.8°	57.6°	39.2°	1.3	23.0°	23.8°	-3.1%

Table A.3 Droplet theoretical and experimental data without imposed vibrations on SiO₂ surface

Surface	Volume [μL]	$\omega_{j,res. freq.}$ [Hz]	$\omega_{j,imp. freq.}$ [Hz]	a_0 [g]	α_{theo}	α_{exp}	Error
SiO ₂	20	38.6	34.1	1.3	29.8°	28.2°	5.6%
	30	32.2	30.9	1.3	24.4°	25.2°	-2.9%
	40	28.4	26.3	1.3	18.8°	19.5°	-3.7%

Table A.4 Acoustic model and experimental data for the first resonance mode on SiO₂ surface

Surface	Volume [μL]	$\omega_{j,res. freq.}$ [Hz]	$\omega_{j,imp. freq.}$ [Hz]	a_0 [g]	α_{theo}	α_{exp}	Error
SiO ₂	20	73.8	71.8	1.2	30.7°	31.9°	-3.7%
	30	60.9	59.9	1.0	26.6°	26.3°	1.0%
	40	53.1	53.2	1.2	19.9°	21.9°	-9.1%

Table A.5 Acoustic model and experimental data for the second resonance mode on SiO₂ surface

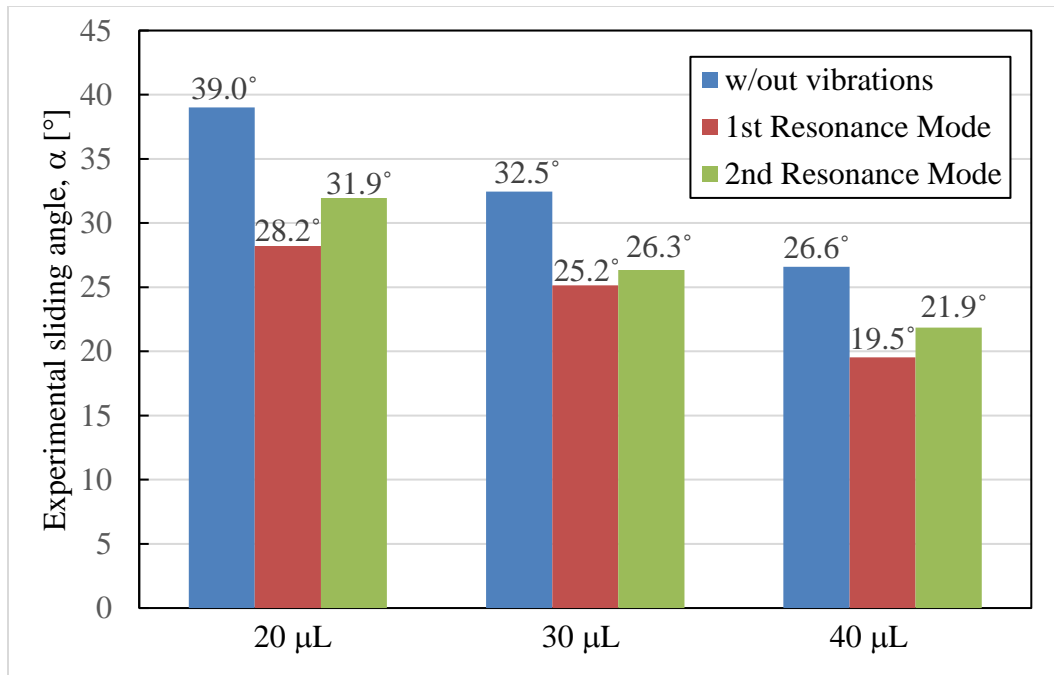


Fig. A.2 The sliding angle of different droplet volumes on SiO_2